Stimulated Raman Scattering and Intermodal Coupling in Continuous-Wave High Power Fiber Lasers

Weixuan Lin

Department of Electrical and Computer Engineering

McGill University, Montreal, Canada

December 2018

A thesis submitted to McGill University in partial fulfillment of the requirements for the degree of Master of Engineering

Abstract

Continuous-wave (CW) high-power fiber lasers (HPFL) are widespread in metal processing applications such as cutting, welding and piercing, because of their excellent beam quality, conversion efficiency and robustness. But the power scalability of HPFLs is significantly limited by nonlinear effects such as stimulated Raman scattering (SRS) and intermodal impairments. This thesis focuses on SRS and intermodal couplings in HPFLs, providing explanations for the mechanisms behind these nonlinear effects and propose suggestions for improving performance of HPFLs.

In terms of the SRS build-up in HPFLs, broadband output-coupler fiber Bragg gratings (OC-FBG) have been found to increase the SRS threshold. In order to understand the mechanism behind the SRS suppression by specific kinds of OC-FBGs, a model based on nonlinear Schrodinger equations (NLSE) is built to simulate the influence of OC-FBGs on HPFLs. In terms of intermodal impairments, intermodal couplings between LP_{01} and LP_{11} modes have been drawing attention of recent studies in high-power amplifiers. In this thesis, a model based on multi-mode general nonlinear Schrodinger equations (MM-GNLSE) is developed and used to simulate intermodal couplings in high-power amplifiers, so that intermodal couplings can be understood and novel phenomena in the presence of intermodal couplings can be investigated.

For master-oscillator power-amplifier (MOPA) systems, the simulation results show that a broader OC-FBG has a better SRS suppression effect. The broadened OC-FBG affects mainly the bandwidth (BW) of the seed laser, and the broadened seed laser mitigates the SRS in the amplifier. But the SRS suppression by broadening the OC-FBG saturates at a point at which strong backward-leakage-power (power leaked through high-reflection FBG) occurs. This is because when strong backward leakage occurs, a broader OC-FBG has little impact on the power and the BW of the seed laser, and thus the SRS threshold is not affected.

For fiber oscillators, simulation results show that a broadband OC-FBG suppresses SRS more efficiently than a narrowband OC-FBG, while it increases the backward leakage power and the initial power of forward propagation. Besides the conventional OC-FBGs, the in-

fluence of chirped-Moire OC-FBG on fiber oscillators is successfully simulated, matching experimental results reported in literature.

Finally, the MM-GNLSE model successfully simulates the intermodal couplings between LP_{01} and LP_{11} in a 25/400 μm YDF, including intermodal four-wave mixing (IM-FWM) and SRS-induced intermodal wave-mixing (IM-WM). Moreover, a second-order high-order mode (HOM) Stokes emerges in the simulation result; this novel phenomenon is a result of the joint effect of IM-FWM and SRS-induced IM-WM. To the best of our knowledge, this is the first work simulating IM-FWM in high-power amplifiers and reporting the second-order HOM Stokes due to intermodal couplings.

Sommaire

Les lasers à fibre de haute puissance (HPFL) à émission continue (CW) sont populaires pour les traitements des métaux tels que le découpage, le soudage et le perçage, en raison de leur excellente qualité de faisceau, de leur efficacité de conversion et de leur robustesse. Par contre, l'accroissement de la puissance des HPFL est considérablement limitée par des effets non linéaires tels que la diffusion Raman stimulée (SRS) et les altérations intermodales. Cette thèse porte sur la SRS et les couplages intermodaux des HPFL, sur l'explication des mécanismes derrière ces effets non linéaires, et propose des suggestions pour accroître la puissance des HPFL.

En ce qui concerne l'accumulation de SRS dans les HPFL, les coupleurs de sortie à base de réseaux de Bragg (OC-FBG) ont pour effet d'accroître le seuil de SRS. Afin de comprendre le mécanisme derrière la suppression de SRS par des types spécifiques d'OC-FBG, un modèle basé sur des équations non linéaires de Schrodinger (NLSE) a été concu à cette fin. En ce qui concerne les dégradations intermodales des HPFLs, les couplages intermodaux entre les modes LP_{01} et LP_{11} ont attiré l'attention des études récentes. Dans cette thèse, un modèle basé sur les équations nonlinéaires généralisées et multimodales de Schrodinger (MM-GNLSE) est développé et utilisé pour simuler des couplages intermodaux dans des amplificateurs de grande puissance, de manière à ce que des couplages intermodaux puissent être compris et de nouveaux phénomènes en présence de couplages intermodaux puissent être examinés.

Par rapport aux systèmes avec oscillateur principal amplifié en puissance (MOPA), les résultats de la simulation démontrent qu'un OC-FBG spectralement plus large produit un meilleur effet de suppression de SRS. L'OC-FBG élargi affecte principalement la largeur de bande de l'oscillateur laser, ce qui a pour effet d'atténuer le SRS dans l'amplificateur. Toutefois, en élargissant l'OC-FBG, la suppression de SRS sature à un point où se produit une accélération de fuite vers l'arrière.

Pour les oscillateurs à fibre optique, les résultats de la simulation démontrent qu'un OC-FBG à bande large supprime le SRS de manière plus efficace qu'un OC-FBG à bande étroite, tout en augmentant la puissance de fuite vers l'arrière et la puissance initiale de propagation

vers l'avant. En plus des OC-FBG conventionnels, l'influence des chirped-Moire OC-FBG sur les oscillateurs à fibre est simulée avec succès, correspondant aux résultats expérimentaux publiés dans la littérature.

Enfin, le modèle MM-GNLSE simule avec succès les couplages intermodaux entre LP_{01} et LP_{11} dans un YDF 25/400 μm, y compris le mélange intermodal à quatre ondes (IM-FWM) et le mélange d'ondes intermodales induit par SRS (IM-WM). De plus, les modes d'ordre supérieurs (HOM) Stokes apparaissent dans le résultat de la simulation. Ce nouveau phénomène résulte de l'effet conjugué de IM-FWM et des IM-FWM induits par SRS. Du meilleur de notre connaissance, il s'agit du premier ouvrage qui simule l'IM-FWM dans des amplificateurs de forte puissance et qui traite du HOM Stokes de second ordre causé par les couplages intermodaux.

Acknowledgement

I would like to thank my supervisor Professor Martin Rochette for his generous support and patient guidance during my master research project. He provides solid knowledge of nonlinear photonics and helps the project a lot. I am also grateful to the opportunities offered by my supervisor.

I also would like to thank Noor Kerem, Li Lizhu, Imtiaz Gabriel, Wasim Firdaus and other colleagues in the nonlinear photonics group. I appreciate their patient discussion and suggestions on the project.

Finally, I am grateful to my mother's support and understanding for these years.

Contents

List of Figures

List of Tables

List of Abbreviations

SRS	Stimulated Raman Scattering
FWM	Four-Wave Mixing
IM-FWM	Intermodal four-wave mixing
Yb^{3+}	Ytterbium ion
Nd^{3+}	Neodymium ion
Ge	Germanium
MOPA	Master oscillator power amplifier
NLSE	Nonlinear Schrodinger equation
MM-GNLSE	Multi-mode general nonlinear Schrodinger equation
YDF	Yb-doped double cladding fibers
HPFL	High power fiber laser
TMI	Transverse mode instability
LD	Laser diode
DCF	Double cladding fiber
GDF	Ge-doped double cladding fiber
NA	numerical aperture
CPS	Cladding power stripper

HR-FBG	High-reflection fiber Bragg grating
OC-FBG	Output-coupler fiber Bragg grating
CM-FBG	Chirped-Moire output-coupler fiber Bragg grating
LMA	Large mode area
PBE	Power balanced equation
SPM	Self-phase modulation
XPM	Cross-phase modulation
ASE	Amplified spontaneous emission
GVD	Group velocity dispersion
FFT	Fast Fourier transform
SSFM	Split-step Fourier method
BW	Bandwidth
HOM	High-order mode
FM	Fundamental mode

Chapter 1

Introduction

This thesis reports on the nonlinear effects in continuous-wave (CW) high power fiber laser (HPFL) systems, including stimulated Raman scattering (SRS) and intermodal impairments. Specifically, the influence of output-coupler fiber Bragg gratings (OC-FBG) on SRS is simulated by a model using nonlinear Schrodinger equations (NLSE); and the intermodal coupling between LP_{01} and LP_{11} is simulated by multi-mode general nonlinear Schrodinger equations (MM-GNLSE). These simulations reveal the details of nonlinear mechanisms in HPFLs and a good understanding of the nonlinear interactions.

1.1 Overview of CW HPFLs

Even though the initial fiber laser design of the sub-watt level targeted telecommunications in the 1960s, fiber lasers have been developed greatly during recent decades. At present, CW fiber lasers have reached high power level as high as 10 kW in the single-mode regime[1], and HPFLs are mature for kW outputs in industry. Its applications are not restricted to telecommunications anymore.

Besides their high power availability, CW HPFLs have the following attractive features [2, 1]:

1. Excellent beam quality: single mode or quasi-single mode can be stably maintained when the systems are operated, compared to some bulk solid-state lasers.

2. High conversion efficiency: both optical-to-optical and electrical-to-optical efficiencies are high.

3. Robustness: the systems are fully fiberized, so that the careful calibration and alignment of free-space components are not needed.

With the above advantages, HPFLs are widely applied in metal processing procedures such as welding, drilling and cutting [2, 1].

To illustrate the general concepts of HPFLs, Fig.1.1 shows a master-oscillator power amplifier (MOPA) system, including a fiber oscillator and a fiber amplifier; MOPA system is one of the typical configurations in HPFL systems. Generally speaking, an HPFL uses laser diodes (LD) as optical pumping sources; utilizes fiber Bragg gratings (FBG) to form an optical oscillator; and uses active fibers, such as Yb^{3+}-doped fibers, to absorb pump power and thus generate (or amplify) lasers at the wavelength determined by the central wavelength of FBGs. Therefore, an HPFL is capable of combining power from multiple LDs into one output beam; converting highly multi-mode optical source from LDs into a quasi-single-mode output beam with excellent beam quality; and converting the wavelength of LDs to the emission wavelength determined by FBGs. In addition, to achieve the aforementioned features of HPFL, double cladding fibers (DCF) are one of the key components in HPFL systems, because these fibers have advantages of high pump absorption rate, lower nonlinear Kerr coefficient and so forth. More detail of DCFs in HPFLs is introduced in Chapter 2.

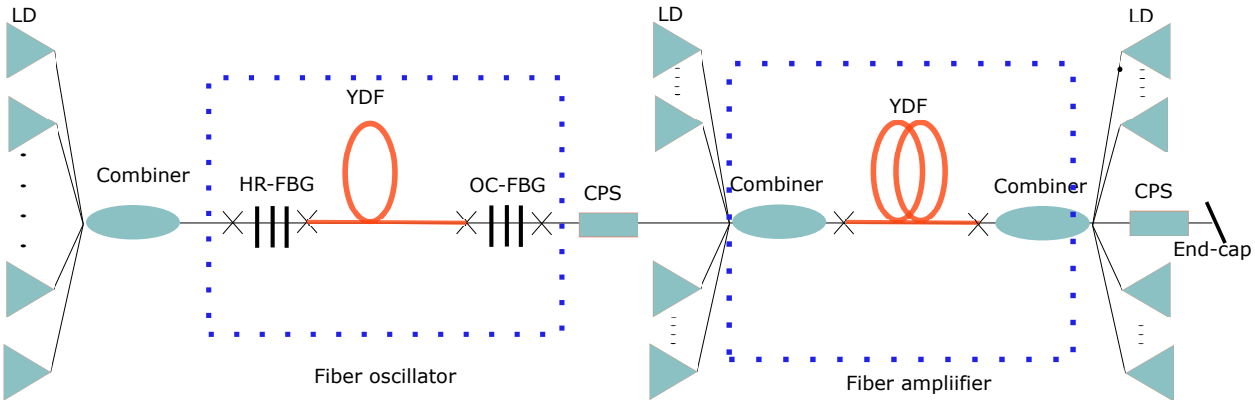

Figure 1.1: Schematic of a typical MOPA system with a bi-pumping amplifier stage. LD: laser diode; HR-FBG: high-reflection FBG; OC-FBG: output-coupler-FBG; YDF: Yb-doped double cladding fiber; CPS: cladding power stripper.

Most of HPFLs operate at emission wavelengths around 1μm. This is because compared to other ranges of wavelengths, most metals exhibit relatively good absorption characteristics at wavelengths around 1μm [3]. The good absorptivity of 1μm wavelength is beneficial to metal processing such as cutting, melting and so forth.

The detail information and characteristics of each component in HPFLs are introduced in Chapter 2.

1.2 Limitations of HPFLs

Even though they are widespread in practice, there are limitations that inhibits the power scaling.

HPFL systems adopt fibers with low value of nonlinear Kerr coefficients [4]. However, because of the high power situation, nonlinear effects inevitably emerge and limit the scaling of output power and the quality of output beams. Among various nonlinear effects, SRS is one of the most significant factors limiting the performance of HPFL systems. SRS can transfer the energy from the emission wavelength to an undesirable Stokes wavelength [5]. More complicated designs of focusing optics are needed for metal processing applications when a strong Stokes wavelength emerges; a strong SRS Stokes can the destabilize the fiber-oscillator in some situations [2]. In addition, when the SRS threshold is reached, the SRS Stokes grows rapidly, seriously deteriorating the output. To enhance the SRS threshold, a number of methods have been researched and proven useful, including the adoption of fibers with larger core-diameters, the adoption of broadband OC-FBGs, and so forth.

Transverse mode instability (TMI) is another significant factor limiting the scalability of output power. When the TMI threshold is reached, energy is exchanged between modes, leading to the instability of the output power and beam quality. The dynamics behind TMI is still not fully clear. The latest explanations of TMI focus on the modal-interference pattern generated by modes and refractive-index grating generated by heat patterns [6, 7, 8], which are proven, experimentally and theoretically, to be linked to the energy transfer between modes. Some conventional methods regarding suppression of TMI are concluded in [9], which includes improving heat management, increasing the high-order mode (HOM) loss, and so

on. Besides, [8, 10] proposed novel methods to achieve TMI suppression by modulating the pump power that are based on the latest TMI theories[6].

1.3 Motivation and Objectives

Since SRS and TMI are two important factors limiting the scalability of output power in HPFL, this thesis focuses on the theories related to the SRS effect and intermodal coupling behaviours in HPFL systems. Specifically, the SRS suppression by OC-FBGs and the intermodal coupling between LP_{01} and LP_{11} are investigated in detail.

One aim of this thesis is to provide a detailed understanding of how OC-FBGs influence SRS threshold in HPFLs. In addition, because the intermodal impairments are increasingly focused in the field of HPFL systems, the other goal of this thesis is to develop and use a model of MM-GNLSE to simulate the intermodal impairments such as intermodal four-wave mixing (IM-FWM) and SRS-induced intermodal wave-mixing (IM-WM). In this way, a detailed understanding of intermodal coupling behaviours is provided.

1.4 List of contents

Chapter 2 introduces some basic concepts in HPFLs, including the configurations, components, absorption/emission cross-sections of Yb-doped double cladding fibers (YDF), and so on. Chapter 3 introduces the simulation models based on NLSE. Chapter 4 uses the model in chapter 3 to simulate HPFL systems with different OC-FBGs. Chapter 5 builds a model based on MM-GNLSE and simulates the intermodal coupling between LP_{01} and LP_{11} in YDFs. Chapter 6 gives the conclusions of this thesis and discusses future works for the improvements of the thesis.

Chapter 2

Background

In this chapter, basic concepts about Yb-doped HPFL are introduced. The characteristics of YDFs are presented.The most important HPFL configurations are compared. As well, every component that serves in a HPFL is presented

2.1 Ytterbium-doped double cladding fibers

2.1.1 Characteristics of Yb^{3+}

Er^{3+}/Yb^{3+}, Tm^{3+}, Yb^{3+} and Nd^{3+} ions are rare-earth dopants widespread in fiber lasers. Er^{3+}/Yb^{3+} and Nd^{3+} doped lasers suffer from relatively large quantum defects and serious thermal issue; Tm^{3+} lasers show their potential in eye-safe kW fiber lasers, but their power scaling is still not comparable to Yb^{3+} doped lasers [2]. Therefore, this thesis focuses only on Yb-doped HPFLs. The most important characteristics of YDF are discussed, such as the choices of pumping and lasing wavelength.

Fig.2.1 shows typical absorption σ_a and emission σ_e cross sections spectra of Yb^{3+} ions in aluminosilicate fibers. For the absorption cross section, two peaks are located at wavelengths 976 nm and 915 nm. The absorption cross section at 976 nm is almost 3 times as large as the one at 915 nm. In addition, σ_a drops rapidly when the wavelength becomes larger than 976 nm. Thus, the adoption of 976 nm has the advantage of the largest absorption rate and thus decreasing the needed fiber length and increasing the SRS threshold. However,

this high absorption rate can cause a heating issue at the same time. Compared to the other pumping wavelengths at 915 nm , 1018 nm or even 1030 nm, pumping at 976 nm has the lowest threshold of TMI [9]. In addition, if non-wavelength-stabilized (NWS) LD are used as pumping sources, because of the temperature's influence on LDs, the output laser's spectra from LDs are inevitably broadened or shifted when the injected current increases. Therefore, the absorption rate may drop when LDs' power reaches certain point. This LD's temperature issue is sensitive when 976 nm pumping wavelength is adopted, because σ_a's peak near 976 nm is especially sharp. For instance, in [11, 12], the efficiency of 1018 nm lasers based on YDF, with the pumping wavelength at 976nm, were largely improved from about 64% to 82%, by replacing the NWS LD to wavelength-stabilized (WS) LD. However, NWS LDs are more commonly used in industrial applications because of their cost compared to WS LDs. Thus, it is a significant issue to choose a proper pumping wavelength.

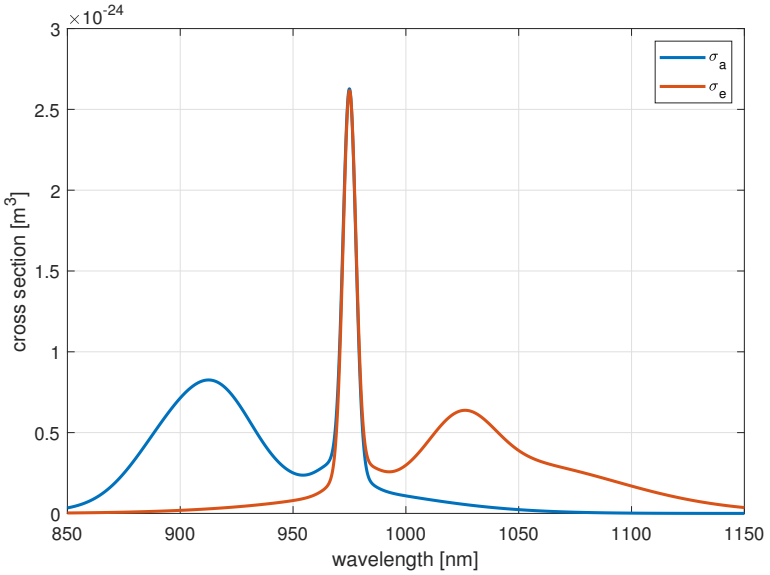

Figure 2.1: Absorption $\sigma_a(\lambda)$ and emission $\sigma_e(\lambda)$ cross-sections spectra of Yb-ion in aluminosilicate fibers.

In terms of emission cross-section, as shown in Fig.2.1, 976 nm and 1030 nm are two emission peaks, and σ_e drops gradually after the peak at 1030 nm. Typically, the lasing wavelengths are usually chosen to be longer than 1064 nm, where the absorption cross section is small, in order to avoid reabsorption effects. Fig.2.2 shows the gain profiles of excitation ratios N_2/N_0 from 10% to 90%, which is calculated by $g \propto [N_2/N_0(\sigma_e+\sigma_a)-\sigma_a]$ [13, 14, 15],

where N_2 is the density of the active atoms in the upper state and N_0 is the total density of the active atoms. The negative values in the gain profile refer to reabsorption effects.

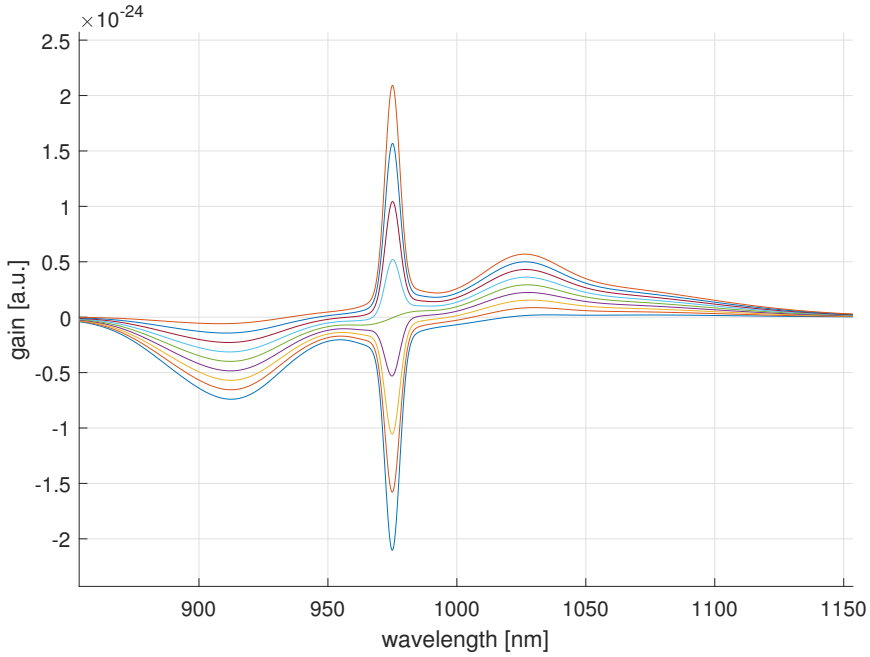

Figure 2.2: Gain profiles of YDF for excitation ratio ranging from 10% to 90% in steps of 10%. The relative gain profiles are calculated as $g(\lambda) = [N_2/N_0(\sigma_e + \sigma_a) - \sigma_a]$ [13, 14, 15], where N_2/N_0 is excitation ratio; σ_a and σ_e are absorption and emission cross-sections spectra, respectively.

The gain profiles show that for lasing wavelengths longer than 1064 nm, a longer wavelength obtains a lower Yb gain. Based on this observation, it is believed that the generation of SRS Stokes can be mitigated by lasing at a longer wavelength, so that the Yb gain at the wavelength of SRS Stokes can be reduced [16]. However, the longer lasing wavelength can increase the temperature along the fiber and reduce efficiency [17]. Thus, choosing a proper lasing wavelength can optimize the system in regard to the problems of reabsorption, SRS , conversion efficiency and so on.

2.1.2 Characteristics of YDF's geometry and refractive-indices

Basic parameters

To better illustrate the concepts in YDFs, important parameters are introduced, including numerical aperture (NA) and normalized frequency (V number), and beam quality factor M^2.

NA for a step-index fiber is defined as

$$\mathbf{NA} = \sqrt{n_{core}^2 - n_{clad}^2} \tag{2.1}$$

where n_{core} and n_{clad} are the refractive indices of the core and the cladding in a step-index fiber, respectively [5]. In YDFs, NA of the core is calculated by using the refractive indices of the core and the inner cladding; NA of the inner cladding is calculated by the refractive indices of the inner cladding and the outer cladding.

Another important optical parameter is normalized frequency, or V number, defined as [5]:

$$V = \frac{2\pi a}{\lambda}\sqrt{n_{core}^2 - n_{clad}^2} = \frac{2\pi a}{\lambda}\mathrm{NA} \tag{2.2}$$

where a is the radius of the core; λ is the wavelength of the light in vacuum. V number measures the mode volume of fibers; a larger V means a larger mode volume in a fiber. For single-mode operation, $V < 2.4048$ is required; the number of modes in a step-index fiber is approximated to $4V^2/\pi^2$. Thus, a larger core radius or an increased NA leads to a larger V value and thus a larger mode volume in the fiber.

Beam quality factor, M^2, denotes how many times faster the beam diverges compared to a diffraction-limited Gaussian beam with the same waist diameter [2]. M^2 is defined as the ratio between beam-parameter product (**BPP**) of the beam and the **BPP** of a diffraction-limited Gaussian beam:

$$M^2 = \frac{\mathbf{BPP}_B}{\mathbf{BPP}_G} = \frac{\omega_B\theta_B}{\omega_G\theta_G} = \frac{\pi}{\lambda}\omega_B\theta_B \tag{2.3}$$

where ω_B and θ_B are the beam's mode-field radius and far-field divergence; λ is the wavelength of the beam; $\mathbf{BPP}_B$ is the **BPP** of the beam to be measured and $\mathbf{BPP}_G$ is the **BPP** of the Gaussian beam. When M^2 is closed to unity, the beam intensity profile appears as a

quasi-Gaussian profile, which is similar with the single-mode intensity profile. A larger M^2 value refers to a deteriorated beam quality. The appearance of HOM degrades the beam quality and thus increases the M^2.

Characteristics

A YDF comprises a core doped with active ions, a cladding , and a outer layer of polymer [18, 2]. Fig.2.3 illustrates the basic structure and the refractive index profile of DCF.

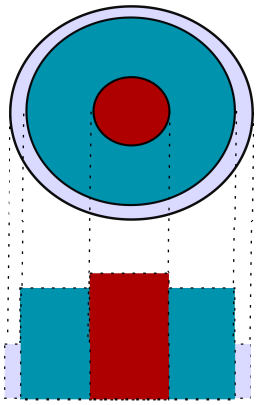

Figure 2.3: A DCF's cross-section (upper figure) and corresponding refractive index profile (bottom figure). The core is shown in red; the inner cladding is in green; the outer cladding is in purple.

The optimal shape of the inner cladding is not necessarily circular, and the core is not necessarily located on the center [2]. Fig.2.4 shows different cross-sections of YDFs [2, 19]. A proper choice of the perturbation of a fiber's cross-section can help maximize mode scrambling, avoid excess scattering loss and increase the pump absorption[2]. However, the perturbation of DCF's cross-section is not further discussed, as it exceeds the scope of this thesis.

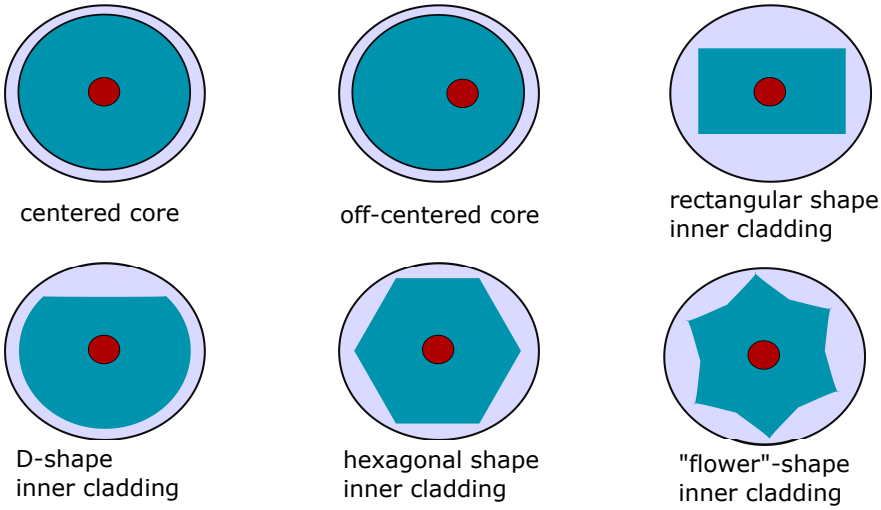

Figure 2.4: Comparison of different DCFs' cross-sections [2, 19]. The core is shown in red; the inner cladding is in green; the outer cladding is in purple.

For the typical commercial YDFs used in studies [2, 20], NA of the core is 0.06; NA of the inner cladding is about 0.46. In terms of the sizes of the fibers, it is common to describe DCFs by their core/cladding diameters ratio such as 20/400 μm, which refer to a DCF whose core diameter is 20 μm and inner cladding diameter is 400 μm. In the market, most popular DCFs have format 20/400 and 25/400 μm.

With a core diameter as large as tens of microns and a core NA as low as 0.06, the purpose of large mode area fiber is to obtain a fundamental mode (FM) with large effective mode area, A_{eff}, while keeping the V number relatively low. In this way, the Kerr nonlinear coefficient, which is proportional to $1/A_{eff}$, remains low to avoid the onset of nonlinear effects. In order to suppress SRS, the core diameters reported in literatures are becoming increasingly large. For instance, Fang successfully built 8 kW LD-pumped MOPA system without the appearance of SRS [21]; in it a 50μm-core YDF was adopted in the amplifier stage. However, the beam quality for this experiment [21] is degraded correspondingly to $M^2 \approx 4$. Furthermore, the adoption of larger core diameter increases the risk of TMI, as the V number is inevitably raised. Therefore, according to the discussion above, the choice of a core diameter should be carefully pondered when designing an HPFL system.

2.2 Typical components and configurations in CW-HPFLs

In this section, important components in HPFL configurations are introduced. The commonly used configurations are presented and compared.

2.2.1 Important components in HPFLs

To demonstrate the basic components in HPFL, a typical MOPA system in [22] is briefly introduced in this section, as shown in Fig.1.1 . For the laser oscillator stage, the power of several LDs is combined by an n-port combiner and the pumping sources are sent into the oscillator from the high-reflection fiber Bragg grating (HR-FBG) end. The seed laser is generated by this oscillator and amplified by a YDF with a bi-directional pumping scheme.

Cladding power strippers

Cladding power strippers (CPS) are used to release unwanted residue light propagating in the cladding. The function of cladding light striping can be achieved by various methods, including the use of high-index polymer recoating, chemical etching, soft metal coating, and laser ablation [23]. For instance, for the early work of CPS, a layer of high-index coating was recoated on a double-cladding fiber, attempting to couple the light out of the cladding [24].

CPSs are necessary components for preventing the cladding light from being coupled into the pump fiber and thereby damaging the LDs. In Fig.1.1, the pump powers in the oscillator stage and amplifier stage are separated by a CPS. On the one hand, for scientific purpose, it is convenient for analysis to separate the oscillator stage and amplifier stage, so that the detail information of the seed laser generated from the oscillator can be detected and the pump power distribution in the amplifier stage can be individually controlled. On the other hand, for industrial purpose, it may be better to make full use of the pump power instead of wasting part of the pump power through CPS. Thus, the MOPA setup with a bidirectional pumping configuration in [25] can be adopted for the entire exploitation of the pump power. Fig.2.5 shows the bidirectional pumping configuration in [25], where the output of the oscillator is directed connected to the input-end of a YDF. In this configuration, the LDs' power have an influence on both stages in the MOPA system. For setups such as

Fig.2.5, the detail information of the seed laser, which is generated by the master oscillator, is not easy to be acquired in the experiment, but in the meantime, the pump power can be exploited entirely.

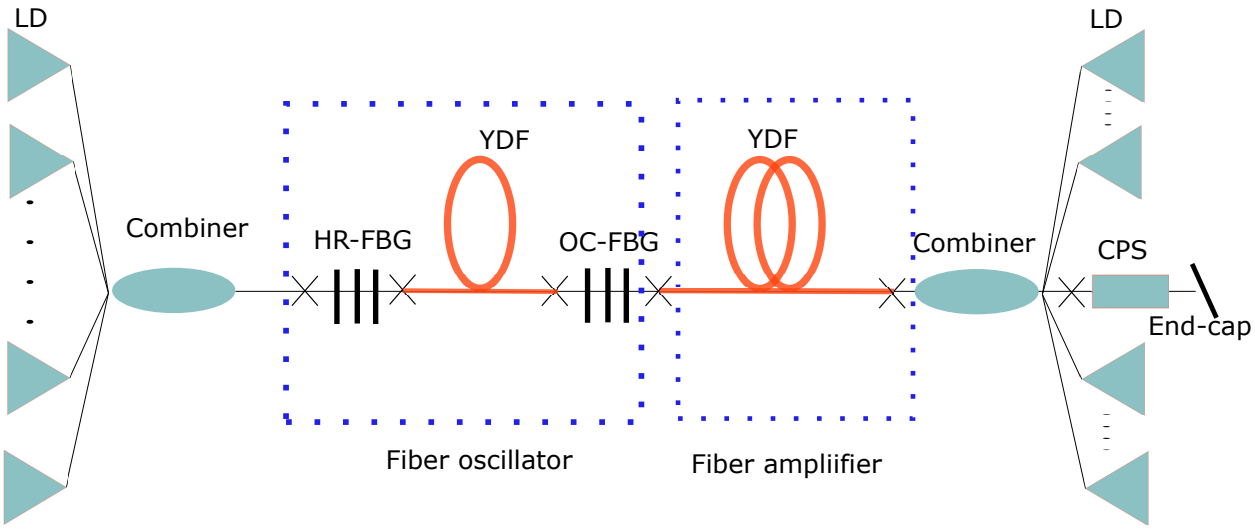

Figure 2.5: Schematic of the bi-pumping MOPA system in [25].

Splices and FBGs

The black crosses in laser setup figures refer to the splices connecting different fiber parts. An imperfect splice may introduce unwanted loss and excitation of HOM [26], so it is necessary to minimize the number of splices in an HPFL system. However, most FBGs written in LMA fibers have to be inscribed in Ge-doped fiber. This inscription technique takes advantage of the photosensitivity of Ge-doped fiber [27]. Thus, splices between GDF-FBG and YDF are necessary in most situations. Even though FBG inscription techniques are highly mature in telecommunications, the inscription techniques for LMA FBG are still challenging. Especially, the fabrication techniques for FBG directly written in active fibers is a recent research domain using femto-second lasers [28, 29, 30, 31].

Pump combiners

Cladding pumping schemes can be categorized mainly into either end-pumping schemes or side-pumping schemes [2].

On the one hand, the end-pumping schemes are simpler but have restrictions on their

performance and scalability [32]. On the other hand , the side-pumping schemes can improve the uniformity of the pump power distribution so that the heat management is improved [32, 2].

Different kinds of cladding pumping schemes require different kinds of pump-combiners. The common pump combiners are designed to be fused tapered fiber bundles or tapered fused bundles (TFB) [32]. However, with this TFB design, only the simple end-pumping system can be achieved. More complex pump combiners are needed for realizations of side-pumping schemes [33, 32, 2].

The detail of the techniques of a variety of pumping schemes is not further discussed in this chapter, since it exceeds the scope of this thesis.

2.2.2 Comparison between different configurations

The configurations of fiber oscillators and MOPAs are two kinds of commonly used structures in HPFL systems.

Fiber oscillators are one kind of the most commonly used configurations. Fiber oscillators have the advantages of shorter effective length, easier manipulation, fewer components and simple structure for pump combiners [34, 25]. But the power scalability of fiber-oscillators is more vulnerable to SRS than MOPA configurations [34], because both forward-propagation light and backward-propagation light in the oscillators suffer from nonlinear effects. Fiber-oscillators are also found to have a lower TMI threshold in studies [25].

2.2.3 Comparison between different pumping schemes

The choice of the pumping scheme is significant in designing a HPFL system. Typically, co-pumping, counter-pumping and bi-directional pumping (bi-pumping) schemes are commonly adopted.

Among these three schemes, counter-pumping and bi-pumping schemes are more difficult to achieve [35, 12]. The challenge is that the strong counter-propagation light may be coupled into pump fibers and damage LD devices. Thus, the backward light coupled into the pump fibers has to be carefully dealt with. One of the methods is to use long active fibers to assure

that the pump power residue is small enough at the pumping ports. Improvements in the coupler components are also made in order to suppress the backward light coupled into the pump fibers [35].

Different pumping schemes were compared in studies [22, 36, 16, 37, 38]. Especially, the comparison between co-pumping and bi-pumping schemes was focused by researchers. Some advantages exhibit on bi-pumping systems. For instance, the bi-pumping system have a better heat management, because the pump power distributes more uniformly along the fiber. In addition, the pump power from each end can be flexibly tuned in order to improve the heat load distribution. And more interestingly, TMI threshold was found to be increased by using bi-pumping scheme. The theoretical detail behind the TMI suppression by bi-pumping is still not fully clear. The uniform heat distribution is believed to be the reason for TMI suppression[9].

2.2.4 Raman effect in HPFL

In a molecular medium, a fraction of the power of a optical filed When an optical field propagates in a molecular medium, a fraction of the power of the field is transferred to a downshifted frequency by spontaneous Raman scattering; the amount of the downshifted frequency is determined by the vibrational modes of the medium [5]. For the perspective of quantum mechanic, this effect can be described as the conversion by a photon $\hbar\omega_p$ to a lower frequency photon $\hbar\omega_s$ by the molecule. A $\hbar\omega_p$ photon excites the molecule to a virtual state; then the molecule transits to a vibrational state and a $\hbar\omega_s$ photon is released in the meantime[5]. The nonlinear phenomenon SRS occurs when the power of the signal light is rapidly transferred to Raman-Stokes light. For silica-glass fiber, the typical amount of the downshifted frequency by Raman effect is 13.2 THz.

For passive fibers, the SRS threshold power is approximately proportional to the effective mode area, A_{eff}, and the reciprocal of effective fiber length, $1/L_{eff}$ [5]. In CW-HPFL systems, besides effective mode area and effective length, it is found that the bandwidth of a optical field propagating in an active fiber can influence the SRS-threshold. Specifically, for a fiber amplifier, a narrowband seed laser has a lower SRS-threshold than the broadband seed [42]; narrowband OC-FBGs can lower the SRS-threshold in HPFL systems, including

single-oscillators and MOPA systems [20, 41].

2.3 Conclusion

This chapter introduced necessary background information regarding HPFL systems. Important components were introduced in detail. Different configurations were introduced and compared.

Chapter 3

Models of CW-HPFLs

Conventionally, power balanced equations (PBE) are utilized to simulate SRS in CW lasers [5, 13]. However, as this model loses the phase information in the laser, it is difficult to simulate the spectral effects. Thus, by using PBE-based models, it is not convenient to simulate SRS suppression phenomenon by specific OC-FBGs reported in experiments [39, 15].

The other hand, NLSE, which take the phase information into account, are widely used to describe the propagation of pulses in $\chi^{(3)}$ nonlinear dispersive media, especially in silica fibers [5]. Recent years, instead of PBEs, NLSEs are applied in modelling CW-HPFL systems [40, 41, 42, 43, 15], and their simulation results agree excellently with experiments.

In this chapter, to demonstrate the similarity and difference between these two models, the model using PBEs and the one using NLSEs are demonstrated and compared.

3.1 Models using power balanced equations

Conventionally, when modelling a CW fiber laser, the temporal features of light are ignored. Thus, nonlinear effects such as SPM and XPM are usually not considered [5, 13, 18]. Simulations by this kind of model focus mainly on the changes of optical powers in different frequencies. To understand the idea of PBE-based models for laser oscillators or amplifiers, a typical model based on PBE in [13] is introduced in this section. The following equations describe the model for a bidirectionally pumping fiber amplifier [13].

Excitation ratio equation:

$$\frac{dN_2(z,t)}{dt} = \frac{\Gamma_p \lambda_p}{hcA}[\sigma_a(\lambda_p)N_1(z,t) - \sigma_e(\lambda_p)N_2(z,t)][P_p^+(z,t) + P_p^-(z,t)] - \frac{N_2(z,t)}{\tau} \quad (3.1)$$

$$N = N_1(z,t) + N_2(z,t) \quad (3.2)$$

Pump depletion equations:

$$\pm\partial_z P_p^{\pm}(z,t) + \frac{1}{\nu_p}\partial_t P_p^{\pm}(z,t) = -\Gamma_p[\sigma_a(\lambda_p)N_1(z,t) - \sigma_e(\lambda_p)N_2(z,t)]P_p^{\pm}(z,t) - \alpha_p P_p^{\pm}(z,t) \quad (3.3)$$

Evolution of signal powers in different channels:

$$\pm\partial_z P^{\pm}(z,t,\lambda_k) + \frac{1}{\nu}\partial_t P^{\pm}(z,t,\lambda_k) = \Gamma[\sigma_e(\lambda_k)N_2(z,t) - \sigma_a(\lambda)N_1(z,t)]P^{\pm}(z,t,\lambda_k) - \alpha(\lambda_k)P^{\pm}(z,t,\lambda_k) + 2\sigma_e(\lambda_k)N_2(z,t)\frac{hc^2}{\lambda_k^3}\Delta\lambda + S\alpha_{RS}(\lambda_k)P^{\mp}(z,t,\lambda_k) \quad k = 1,...K \quad (3.4)$$

Among these equations, $N_2(z,t)$, $N_1(z,t)$ and N are upper-level populations, ground-level populations and Yb dopant concentration, respectively; σ_a and σ_e are absorption and emission cross sections, respectively; Γ are overlap area between dopant area and signal or pump; $P^{\pm}$ is the power of signal light propagating forwardly or backwardly; τ is the life-time of Yb-ions; $P_p^{\pm}$ is the forward or backward pump power; ν_p is the group velocity of pump light; ν is the group velocity of signal light; h is Plank constant; c is the speed of light; A is the dopant area; α_{RS} is the Rayleigh scattering coefficient; S is the capture factor of the fiber core; $\Delta\lambda$ is the bandwidth of ASE.

In this model, the evolution of the upper-level population along the fiber is considered in Eqs.(3.1) and Eqs.(3.2); pump depletion results from pump absorption and background loss as described in Eqs.(3.3); besides, Eqs.(3.4) considers the Yb-ion gain $g(\lambda_k) = \Gamma[\sigma_e(\lambda_k)N_2(z,t) - \sigma_a(\lambda)N_1(z,t)]$, background loss for different frequencies $\alpha(\lambda_k)$, ASE and Rayleigh scattering. Powers in different frequencies are written as $P(z,t,\lambda_k)$.

It should be noticed that nonlinear effects, such as SRS, XPM and SPM, are not included

in this PBE-based model. In the framework of PBE-based models, SRS can be modelled by adding an additional frequency channel at the Stokes frequency so that power can be transferred from the emission light to the Stokes with the Raman gain coefficient g_R [5, 18]. The additional PBE for the Stokes wavelength can be expressed as

$$\frac{d}{dz}P_{Stokes}(z) = \frac{g_R P_{emission}(z)}{A_{eff}} + g(\lambda_{Stokes})P_{Stokes} - \alpha_s P_{Stokes} \tag{3.5}$$

where the first term on the right-hand-side is Raman gain, the second is Yb-ion gain and the last is background loss; $P_{Stokes}(z)$ is the SRS Stokes power along the distance; g_R is Raman gain coefficient; $g(\lambda_{Stokes})$ is the Yb-ion gain on SRS Stokes wavelength; α_s is the background loss.

3.2 Models using NLSEs

In this section, the model for co-pumping oscillator is introduced and then the amplifier model is demonstrated.

3.2.1 A brief introduction to NLSE

In the field of nonlinear fiber optics, NLSEs are commonly utilized to describe the propagation of light in silica fibers [5]. Starting with the Maxwell equations and the boundary conditions of a single-mode step-index fiber, a directional pulse-propagation equation is generalized to the NLSE in [5]. NLSE describes the evolution of the complex amplitude of a pulse along the fiber. Generally speaking, the NLSE for a single-mode passive fiber can be written in the form as [5]: $\partial_z A = \hat{D}A + \hat{N}A$, where $\hat{D}$ represents the dispersion effect and $\hat{N}$ the nonlinear effect. By employing this equation, a number of nonlinear effects can be simulated, including SPM, XPM, SRS, FWM.

To use NLSE to model an active fiber, it is necessary to complement a gain term G in the NLSE, leading to a NLSE in the form of $\partial_z A = \hat{D}A + \hat{N}A + \hat{G}A$. In the earlier NLSE-based CW laser model [43], the Yb-ion gain was calculated based on effective two-level rate equation and pump-depletion equation, so that the NLSE can obtain a Yb-ion gain as same

as the one in the model based on PBE. However, in this work [43], only the gain at emission wavelength was calculated. For the works in recent years [40, 41, 42] , although the same principle of effective two-level rate equation was used, the wavelength-dependent gain was introduced, and thus the model became more intuitive and closer to the experiment in reality.

3.2.2 Models of co-pumping oscillators and amplifiers

The lasing process in a fiber cavity can be regarded as a boundary condition problem, which can be solved by a reciprocal amplification of an optical field along a active fiber while FBGs act as filters. Based on this idea, [43, 41, 15] utilized iterative models to simulate Yb-doped oscillators. In the oscillator model, as demonstrated in Fig.3.1, for each iteration, forward-propagation field, $A^+(z,t)$, and backward-propagation field, $A^-(z,t)$, propagate along a active fiber by opposite directions; after OC-FBG filters $A^+(z,t)$ at the output-end of the fiber, the initial condition of the backward-propagation is determined; after HR-FBG filters $A^-(z,t)$ at the input-end of the fiber, the initial condition of the forward-propagation is determined for the next iteration.

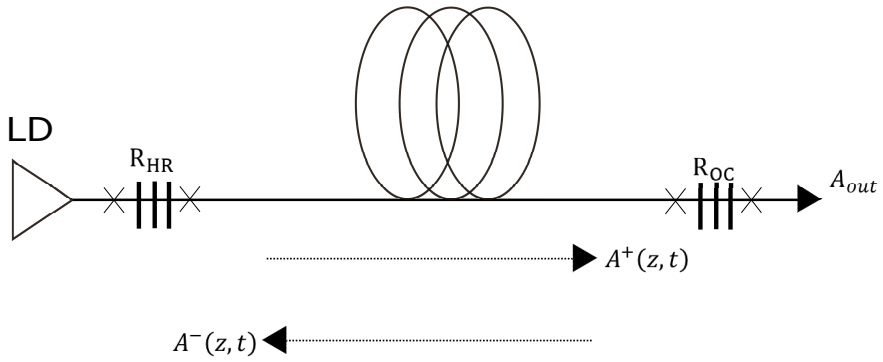

Figure 3.1: Schematic of a model for a co-pumping single-cavity laser.

The propagation of optical fields (forward-propagation $\tilde{A}^+(z,\omega)$ or backward-propagation $\tilde{A}^-(z,\omega)$) inside a cavity are depicted by NLSEs as

$$\pm\frac{\partial}{\partial z}\tilde{A}^{\pm}(z,\omega) = \frac{1}{2}[g(\omega)-\alpha(\omega)] + i\sum_{n=2}^{3}\frac{\beta_n}{n!}\omega^n\tilde{A}^{\pm}(z,\omega) + i\gamma F\{\tilde{A}^{\pm}(z,\omega)[R(t)\otimes|A^{\pm}(z,t)|^2]\} \tag{3.6}$$

where $g(\omega)$ and $\alpha(\omega)$ are the wavelength-dependent gain and background loss ,respectively; β_2 and β_3 are the second and the third order group velocity dispersion (GVD); γ is the Kerr nonlinear coefficient; $R(t) = (1 - f_R)\delta(t) + f_R h(t)$ includes SPM effect and SRS, where Raman response $h(t) = \frac{\tau_1+\tau_2}{\tau_1\tau_2^2}\exp(-t/\tau_2)\sin(t/\tau_1)$ and f_R is the fraction of Raman effect [5].

The wavelength-dependent gain $g(\omega) = \Gamma_s\{[\sigma_a(\omega) + \sigma_e(\omega)]N_2 - \sigma_a(\omega)N_0\}$ is controlled by the effective two-level rate equations, which include a pump-depletion Eqs(3.7) and an excitation-ratio equation Eqs(3.8), respectively.

$$\frac{d}{dz}P_p(z) = -\Gamma_p\{\sigma_a(\omega_p)N_0 - (\sigma_a(\omega_p) + \sigma_e(\omega_p))N_2\}P_p(z) - \alpha_p P_p(z) \tag{3.7}$$

$$\frac{N_2}{N_0} = \frac{\frac{\Gamma_p}{\hbar\omega_p A}\sigma_a(\omega_p)P_p + \frac{1}{2\pi T_m A}\int\frac{\Gamma_s}{\hbar\omega}\sigma_a(\omega)(|\tilde{A}^+(z,\omega)|^2 + |\tilde{A}^-(z,\omega)|^2)d\omega}{\frac{\Gamma_p}{\hbar\omega_p A}[\sigma_a(\omega_p) + \sigma_e(\omega_p)]P_p + \frac{1}{\tau} + \frac{1}{2\pi T_m A}\int\frac{\Gamma_s}{\hbar\omega}[\sigma_a(\omega_p) + \sigma_e(\omega_p)](|\tilde{A}^+(z,\omega)|^2 + |\tilde{A}^-(z,\omega)|^2)d\omega} \tag{3.8}$$

where $\sigma_a(\omega)$ and $\sigma_e(\omega)$ are the absorption cross section and the emission cross section of Yb, respectively; Γ is the overlap factor; N_0 is the Yb dopant concentration, N_2 is the total number of excited Yb-ion; $\hbar$ is the Planck's constant ; T_m is the time window width of the FFT; A is the effective mode area of the field in the fiber; P_p is the power of the pump; $\otimes$ represents the convolution operation and $F\{\cdot\}$ is the Fourier transform.

The boundary conditions in a fiber oscillator are expressed as

$$\begin{aligned}\tilde{A}^+(0,\omega) &= \sqrt{R_{HR}(\omega)}\tilde{A}^-(0,\omega)\\ \tilde{A}^-(L,\omega) &= \sqrt{R_{OC}(\omega)}\tilde{A}^+(L,\omega)\end{aligned} \tag{3.9}$$

where R_{HR} and R_{OC} are reflectivity spectral profiles of HR-FBG and output-coupler (OC) FBG, and L is the length of the oscillator. The output of the oscillator is shown as

$$\begin{aligned}\tilde{A}_{out}(L,\omega) &= \sqrt{1 - R_{OC}(\omega)}\tilde{A}^+(L,\omega)\\ P_{out} &= \langle|A_{out}|^2\rangle\end{aligned} \tag{3.10}$$

where $\langle\cdot\rangle$ refers to the averaging in time; $\tilde{A}_{out}$ is the output field in frequency space; P_{out} is the output power.

In terms of the model for co-pumping amplifiers, by setting $\tilde{A}^{-}(z,\omega) = 0$, the same equations from Eqs.3.6 to Eqs.3.8 can be used to represent the amplification and nonlinear process of a unidirectionally-propagating optical field in a co-pumping amplifier.

3.2.3 Post-processing

The iterative oscillator model described above has outputs varying from iteration to iteration [20]. Thus, a number of iterations from the oscillator model outputs have to be recorded for post-processing so that it leads to stable and reproducible outputs [20].

Assuming n iterations are recorded for post-processing, power versus time $P(t)$, power spectral density$\tilde{P}(\omega)$, and SRS ratio are defined by the following equations. The SRS ratio is defined as the ratio between power located in the SRS Stokes wavelength λ_{Stokes} and the power of the whole.

$$P(t) = \frac{\sum_1^n |A_n(t)|^2}{n} \tag{3.11}$$

where $A_n(t)$ refers to the n^{th} recorded output field in temporal space, $P(t)$ is the average output power in temporal space.

$$\tilde{P}(\omega) = \frac{\sum_1^n |\tilde{A}_n(\omega)|^2}{n} \tag{3.12}$$

where $\tilde{A}_n(\omega)$ refers to the n^{th} recorded output field in frequency space, $\tilde{P}(\omega)$ is the average power spectral density.

$$\text{Raman} \quad \text{Ratio} = 10\log_{10}\frac{\int_{\omega_{\text{Stokes}}}\tilde{\text{P}}(\omega)\text{d}\omega}{\int\tilde{\text{P}}(\omega)\text{d}\omega} \quad [\text{dB}] \tag{3.13}$$

where ω_{Stokes} is the frequency range of SRS Stokes.

3.2.4 Algorithm for numerical computation

The split-step Fourier method (SSFM) is a widely used algorithm to solve the NLSE numerically [5]. For the NLSE in a passive fiber, $\partial_z A = \hat{D}A + \hat{N}A$ can be approximately solved based on the mathematical relation

$$A[z + \Delta z] \approx \exp(\hat{N}\Delta z)\exp(\hat{D}\Delta z)A[z] \tag{3.14}$$

This equation means that a propagation step for a pulse can be divided into a segment of nonlinearity $\exp(\hat{N}\Delta z)$ and another segment of dispersion $\exp(\hat{D}\Delta z)$.

An exponential operator $\exp(\Delta z\hat{D})$ containing operator ∂_t can be evaluated in Fourier space $\hat{D}(-i\omega)$ by

$$exp(\Delta z\hat{D})A(z,t) = F_T^{-1}\exp[\Delta z\hat{D}(-i\omega)]F_T A(z,t) \tag{3.15}$$

where F_T and F_T^{-1} are Fourier transform and inverse Fourier transform, respectively. $\hat{D}(-i\omega)$ is obtained from replacing ∂_t in $\hat{D}$ by $-i\omega$. For instance, $\hat{D} = \frac{\beta_2\partial^2}{2\partial t^2} + \frac{\beta_3\partial^3}{6\partial t^3}$ can be transformed into Fourier space $\hat{D}(-i\omega) = \frac{\beta_2(-i\omega)^2}{2} + \frac{\beta_3(-i\omega)^3}{6}$. By the above principle, it is convenient and intuitive to propagate every step either in frequency space or time space.

To improve the accuracy of SSFM, a symmetric form of exponential operators in Eqs.3.16 is commonly used in computation, in which a different procedure to propagate a pulse is adopted [5].

$$A[z + \Delta z] \approx \exp(\hat{D}\frac{\Delta z}{2})\exp(\hat{N}\Delta z)\exp(\hat{D}\frac{\Delta z}{2})A[z] \tag{3.16}$$

The SSFM algorithm for solving the NLSE amplifier model is illustrated in Fig.3.2. The amplifier model can be expressed in a NLSE in the form as $\partial_z A = \hat{D}A + \hat{N}A + \hat{G}A$, which refers to dispersion, nonlinearity and net gain, respectively. In each step of the iterations, the field first experiences a half step of dispersion effect, then a full step of nonlinearity, a half step of dispersion effect and finally a full step of gain. Besides, in every iteration, the excitation ratio N_2/N_0 and pump power P_p have to be updated by Eqs.(3.8) and Eqs.(3.7).

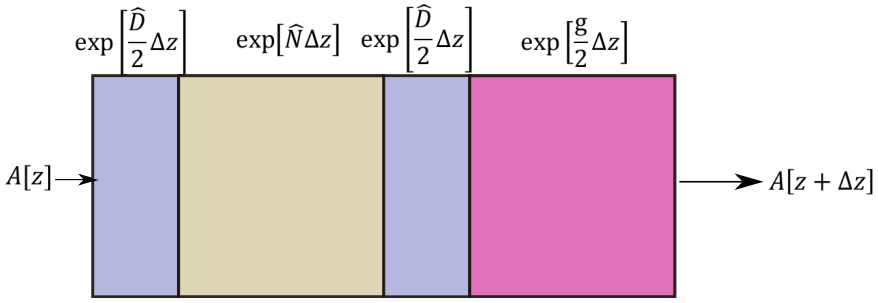

Figure 3.2: Schematic of SSFM for solving the amplifier model in the form as $\partial_z A = \hat{D}A + \hat{N}A + \hat{G}A$.

The algorithm for the iterative oscillator model is shown as follow.

(i) Determine initial condition of forward propagation $A^+(z=0,t)$ as white noise;

(ii) Calculate the propagation of $A^+(z,t)$ by using Eqs.(3.6), Eqs.(3.7) and Eqs.(3.8); update and record the excitation ratio N_2/N_0 along the fiber distance;

(iii) Obtain initial condition of backward propagation $A^-(z=L,t)$ by using boundary condition Eqs.(3.9);

(iv) Solve backward propagation $A^-(z,t)$ using Eqs.(3.6). The gain is governed by the N_2/N_0 recorded in procedure (ii);

(v) Obtain initial condition of forward propagation by Eqs.(3.9); go to procedure (ii) until the output power converges.

In the model, the excitation ratio along the fiber $N_2(z)/N_0$ is only updated during forward propagations. The updated excitation ratio is used to calculate the gain profiles for the backward propagation.

3.2.5 Temporal features in Yb-doped fiber lasers

The NLSE-based model assumes the quasi-CW nature of the light generated by Yb-doped fiber laser. For the simulation outputs from this kind of model, there are a series of pulse-like temporal "features" [44].

A 0.5 ns time duration is used in the simulation for demonstration of the temporal features for different BWs. Fig.3.3 and Fig.3.4 show the temporal domains and frequency domains of two lasers generated by the cavity model, where the normalized intensity is defined as the intensity divided by the mean power $|A|^2/\langle|A|^2\rangle$. Comparing Fig.3.3 and Fig.3.4, for the generated laser with a narrower BW, the pulse-like features in temporal domain are longer but fewer, which agrees with the description in studies [44, 42].

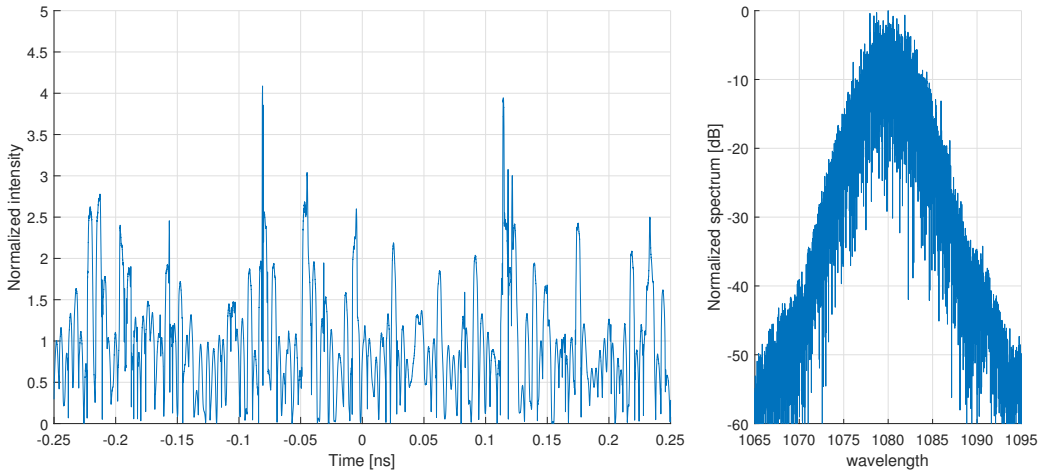

Figure 3.3: Temporal features (left) of the laser with a broadband spectrum (right).

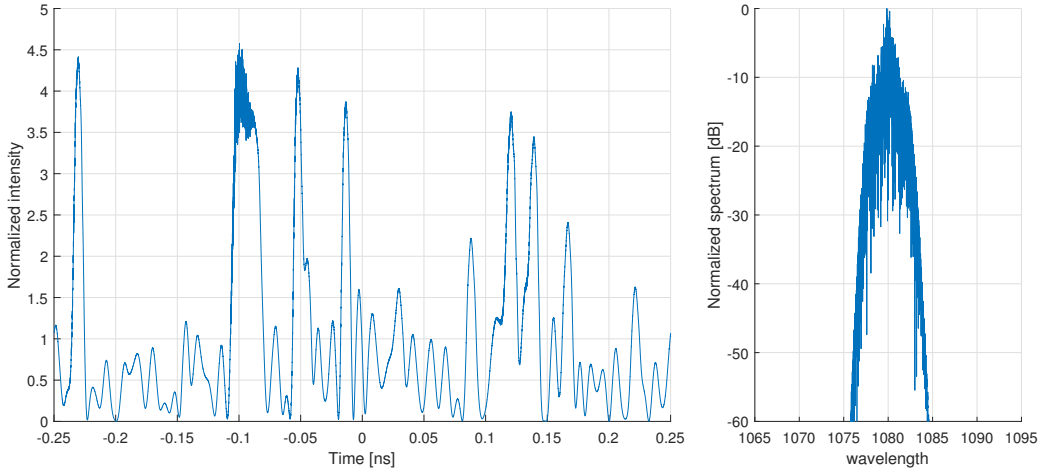

Figure 3.4: Temporal features (left) of the laser with a narrowband spectrum (right).

In terms of experiments, [45] proved the quasi-CW nature of Yb-doped narrowband fiber lasers. In [45], a Yb-doped fiber laser with 2.6 GHz BW was measure in real-time.

Furthermore, by using NLSE-based cavity model, the simulation laser output had a auto-correlation function (ACF) similar with the experimental measurement's ACF. Therefore, this study [45] proved quasi-CW nature of Yb-doped fiber lasers experimentally.

3.3 Conclusion

Compared with the model based on NLSE, the PBE model shares the same part of pump-depletion equation and excitation-ratio equation. So, the PBE model can be regarded as the power evolution part in the NLSE model. By the uses of FFT window, the NLSE-based model avoids to build multiple channels as PBE-based model does. In addition, with the help of NLSE and SSFM, the energy exchange between frequencies due to nonlinear effects is calculated in a more convenient and physical-intuitive way, while PBE-based model is inconvenient to model nonlinear effect because of the absence of the phase information.

Although the assumption behind the NLSE-based amplification model [43, 41] is contrary to the conventional CW laser modelling [13, 5], the nature of quasi-CW of Yb-doped fiber laser was proved experimentally, and the NLSE-based amplification model matched the experimental measurement's ACF [45] as well.

Therefore, the NLSE-based amplification model has advantages compared to PBE-based model, and the NLSE-based model was validated experimentally in [45]. In the following chapters, NLSE-based models are applied to the simulations and analysis of various phenomena in Yb-doped CW HPFLs.

Chapter 4

Influence of the OC-FBG on the SRS build-up

Researchers have been focused on OC-FBGs in CW-HPFLs since [15] found that a broad OC-FBG can have certain SRS suppression effect. In the early stage of this topic, experimental results and a model based on NLSE were given in [15]; it was found that a broad OC-FBG in a single oscillator design can suppress SRS. After this work, more interesting papers harnessed NLSE-based models to find the factors related to SRS threshold in MOPA systems or single-oscillator systems.

In terms of MOPA systems, by using NLSE-based models, more features influencing SRS threshold in MOPA systems have been found. Liu et al. theoretically found that larger power of the seed laser can lower the SRS threshold [41]. Experiments in study [46] changed the power of seed lasers in a MOPA system and investigated the relation between seed laser power and SRS threshold; the experimental results agreed with the simulation results in [41]. In addition, Liu controlled the bandwidths of seed lasers by using FBGs to filter the superfluorescent source [42]; this study found that a seed laser with a narrower bandwidth (given a constant power) leads to a smaller SRS threshold. The simulation done by the NLSE-based model in [42] agreed with the experimental result. Thus, the features of a seed laser injected into a amplifier, including the power and the bandwidth of the seed, are found to have significant influence on SRS threshold in a MOPA system.

In terms of single oscillator designs, after the earlier the oscillator model presented in [15],

[20] showed the detailed outputs of the NLSE-based oscillator model. In [20], a decreasing SRS threshold was found by a narrower OC-FBG; the output power, round-trip gain and SRS content varied strongly from iteration to iteration when a narrower OC-FBG was adopted in the model.

Besides the conventional OC-FBGs, more special spectral profiles of OC-FBGS were investigated experimentally in study [39]. Especially, chirped-Moire OC-FBGs (CM-FBG), with spectral profiles of multi-peak shapes, were found to be capable of suppressing SRS such as broadband OC-FBGs; in the same time, the backward leakage power was mitigated by using CM-FBGs.

In this chapter, the model built in Chapter 3 is utilized to analyse the influence of OC-FBGs on HPFL systems. By analysing the output features when employing different OC-FBGs in detail, strategies to choose the bandwidths of OC-FBGs are proposed. Furthermore, fiber oscillators with CM-FBGs are simulated; the simulation results agree with the experiment in [39]. To the best of our knowledge, this is the first work to theoretically investigate the influence of CM-FBGs on fiber oscillators.

4.1 Influence of bandwidth of OC-FBG on SRS threshold in MOPA systems

In this section, simulations are done to analyse the impact of OC-FBGs on MOPA systems.

4.1.1 Simulation plan

A co-pumping MOPA configuration, as shown in Fig.4.1 is adopted in simulations. The simulation scheme can be regarded as a combination of a co-pumping cavity and a co-pumping amplifier; all of the pump power is injected from the HR-FBG end, and 100% pump power is assumed to be coupled into the cavity; the residue pump power from the end of the cavity is used as the initial pump power for the YDF, and the output field from the cavity is used as the initial condition of the YDF simulation.

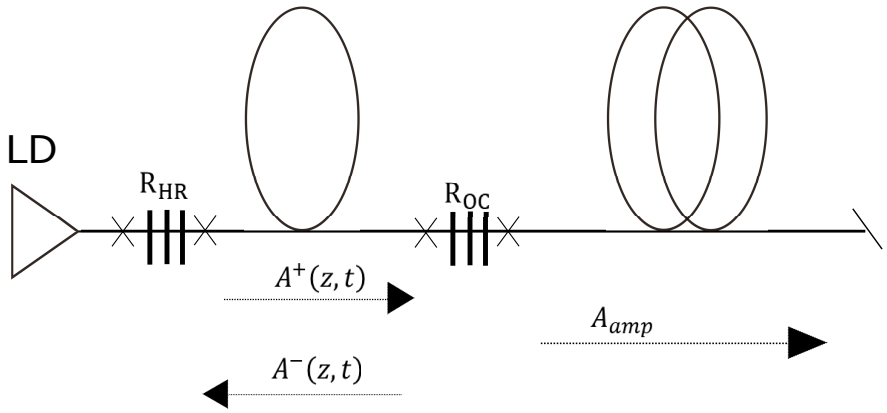

Figure 4.1: Schematic of the model for a co-pumping MOPA system. The algorithm includes an oscillator model (a boundary condition problem) and a YDF model (an initial condition problem).

The major parameters of YDFs in the MOPA simulation are demonstrated in Tab.4.1.

Table 4.1: Parameters for the YDF in the MOPA simulation

Parameter	Value	Parameter	Value
λ_p	976 nm	λ_s	1080 nm
Γ_p	0.0037	τ	0.85 ms
N_0	$3 \times 10^{25}\mathrm{m}^{-3}$	L	20 m
γ	5 W^{-1}/km	Γ_s	0.85
β_2	20.4 ps^2/km	β_3	0.04 ps^3/km

To enhance pump absorption, a pumping wavelength of 976 nm and a 20-meter fiber amplifier whose concentration N_0 equals to $3 \times 10^{25}\mathrm{m}^{-3}$ are adopted. Typical nonlinear coefficient and dispersion parameters for 20/400 μm YDF are employed [41]. The pump power is set to be 3000 W. The oscillator uses the same parameters in Tab.4.1, except that the length of the oscillator is 5 meters. The reflectivity spectral profile of the HR-FBG is modelled as a super-Gaussian with 4 nm full-width-half-maximum (FWHM) and peak equal to 0.995. The shapes of spectral profiles of OC-FBGs are super-Gaussian, and the maximum reflectivities are 10%. Numerous widths of OC-FBGs are employed in the simulations, and their outcomes are compared in the following sections.

Because of the short cavity length in the simulation, the variation of outputs from the cavity is small. Thus, only 2 iterations of the cavity outputs are recorded for post-processing in order to speed up the computation.

4.1.2 Simulation results and discussion

As shown in Fig.4.2, the output power for different OC-FBGs ranges from about 2655 W to 2705 W, and the average power is about 2680 W. Thus, only less than ±1% variation of output power emerges among different OC-FBGs. So, the BW of OC-FBG is considered to have little impact on the output power, and thus the output power is governed mainly by the Yb-ion concentration and the length of the YDF.

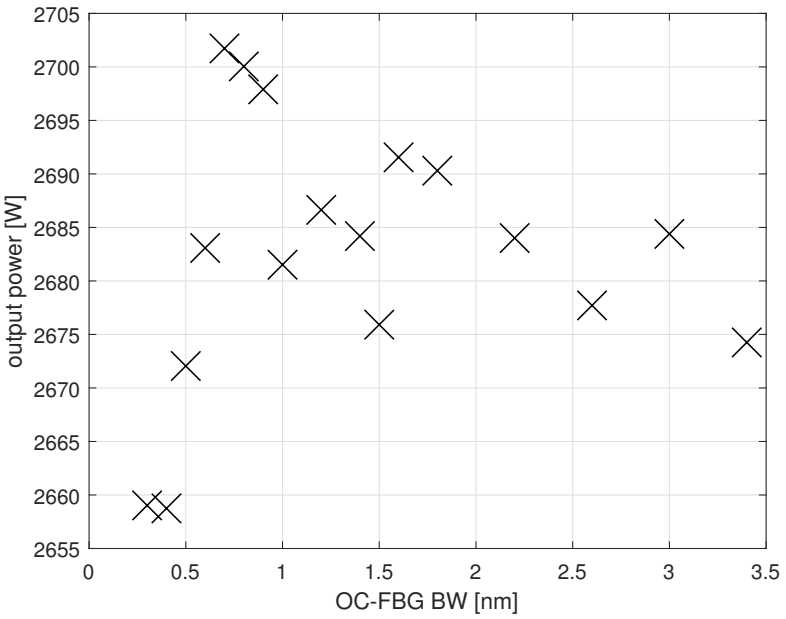

Figure 4.2: Simulation result: output power of MOPA as a function of the BW of the OC-FBG.

The fluctuation in Fig.4.2 comes mainly from the unstable output power from iteration to iteration in the cavity model. This variation of power appears in [20] as well. By increasing the averaging number, the variation of output power can be smoothed, but this will increase the time cost in the computation.

Fig.4.3(a) shows the output power from the cavity of every iteration of all OC-FBGs. The output power of each OC-FBGs converges to around 750 W after the 15^{th} iteration. The variation of output power is smaller when the BW of OC-FBG is larger, as shown in Fig.4.3(b). These also agree with the result in [20].

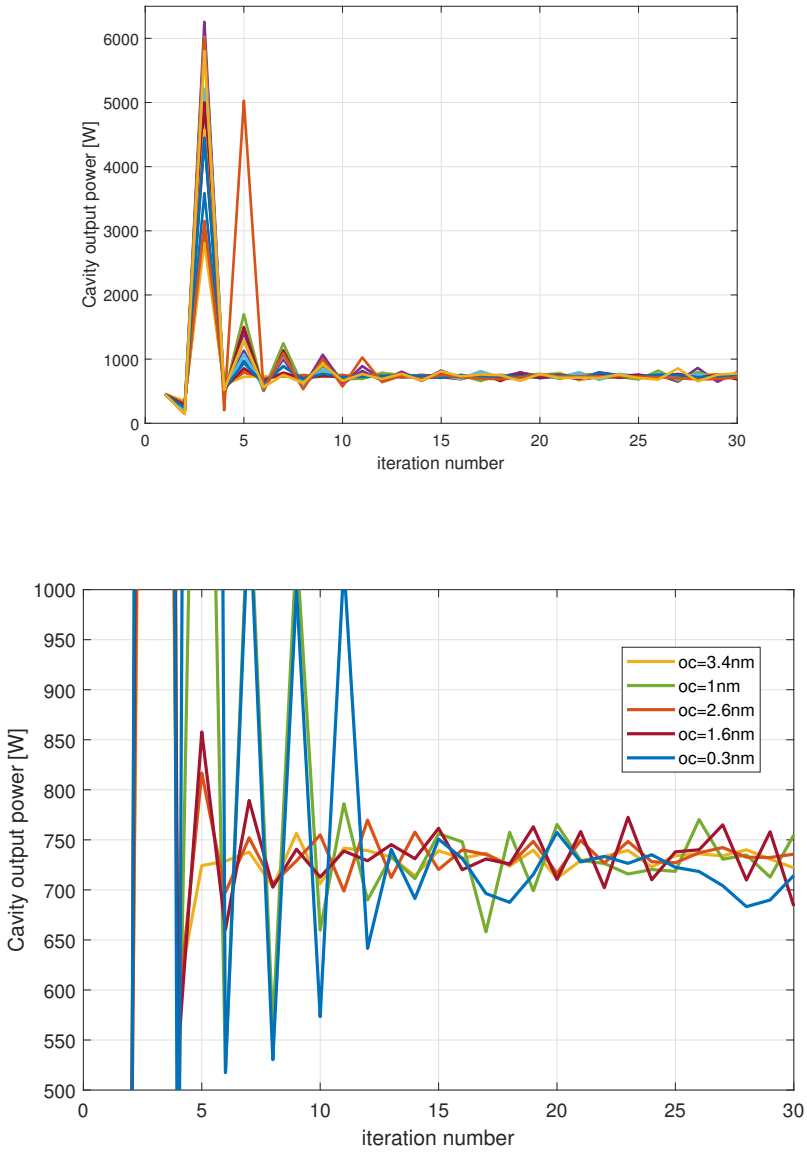

Figure 4.3: output power of the cavity vs iteration number of (upper) all simulated OC-FBGs; (bottom) selected OC-FBGs.

To demonstrate the growth of power in the simulation, Fig.4.4 shows the evolution of optical powers along the fibers and the evolution of excitation ratio along the YDF. The oscillator stage is located from 0 m to 5 m, where the forward propagation power P^+ and the backward propagation power P^- is bounded by FBGs. In the amplifier stage, from 5 m to 25 m in the figure, the pump P_p is fully absorbed; the growth of the signal P_s becomes saturated at the final stage of the amplifier; at the same time, the excitation ratio N_2/N_0 drops from about 11% to about 2.25%.

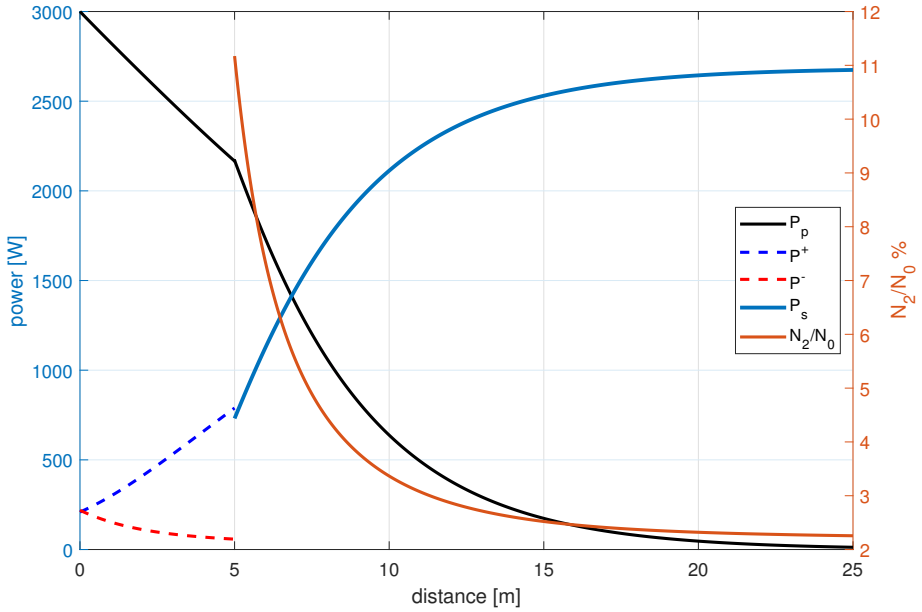

Figure 4.4: Simulation result: evolution of optical powers along the fibers and excitation ratio N_2/N_0 in percentage along the amplifier (OC-FBG's BW = 3.4 nm). P_p is pump power; P^+ is forward-propagation power in the oscillator; P^- is backward-propagation power in the oscillator; P_s is the signal power in the amplifier.

The relation between SRS ratio of output spectra and the BW of OC-FBG are shown in Fig.4.5. The simulation result shows a great improvement of SRS ratio when the BW of OC-FBG increases from 0.3 nm to 1.6 nm, as the SRS ratio drops from about -12 dB to -29 dB. The SRS ratio becomes basically stable at the range from -28 dB to -26 dB when the BW of OC-FBG is larger than 1.6 nm. In other words, the SRS suppression effect saturates when the OC-FBG's BW goes beyond 1.6 nm.

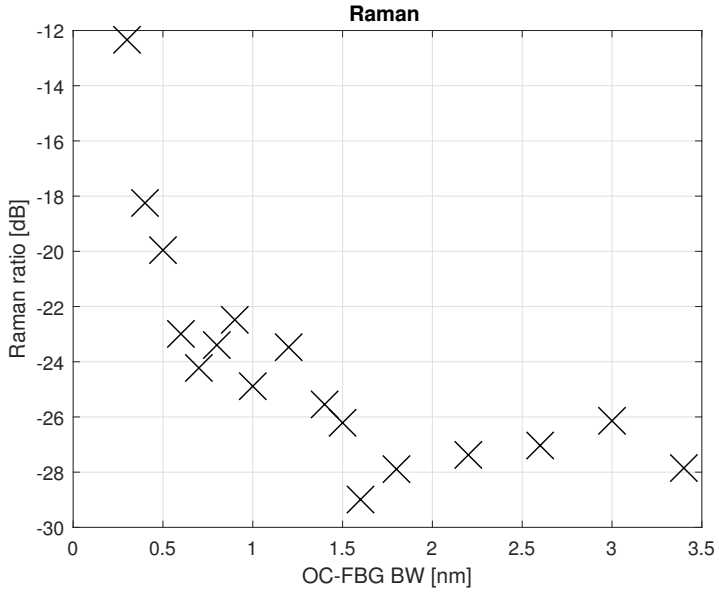

Figure 4.5: Simulation result: SRS ratios of MOPA versus the BW of the OC-FBG.

Fig.4.6 shows some typical output spectra for OC-FBGs with BWs of 0.3, 0.4, 1.6 and 3.4 nm. A broader OC-FBG in a MOPA system broadens the linewidth at emission wavelength (1080 nm), whereas the SRS Stokes at 1034 nm is mitigated.

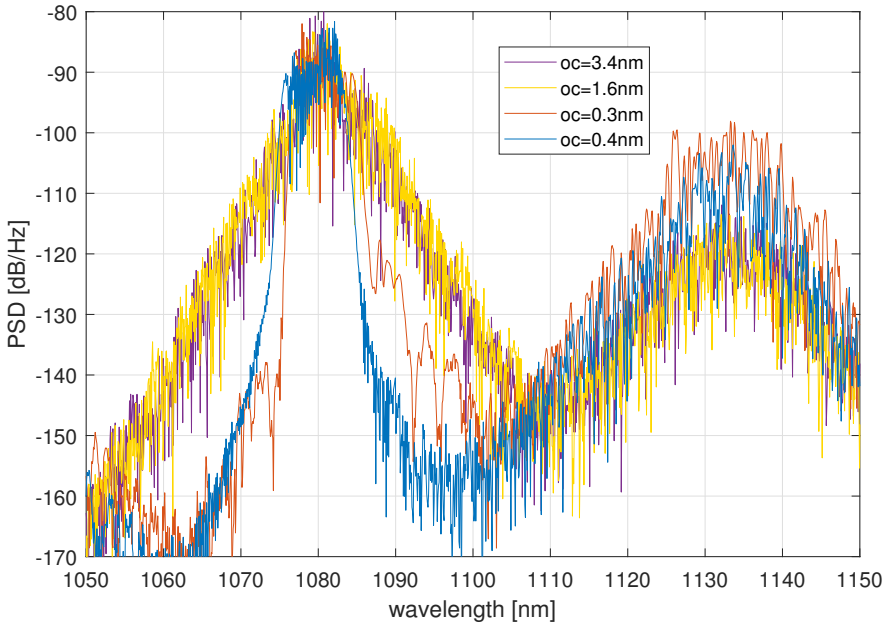

Figure 4.6: Simulation result: Power spectral densities (PSD) of the co-pumping MOPA system using OC-FBGs with the BW of 0.4 nm, 0.4 nm, 1.6 nm and 3.4 nm.

Fig.4.7 shows the relation between the backward leakage power and the BW of OC-FBG. The backward leakage power keeps stable when the OC-FBG has a BW smaller than 1.6 nm. However, the backward leakage power starts to grow exponentially when the BW of OC-FBG is larger than 1.6 nm.

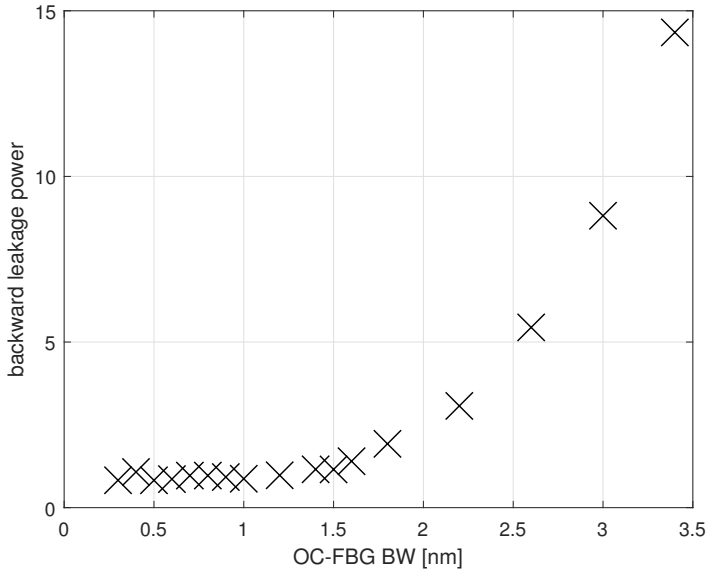

Figure 4.7: Simulation result: backward leakage power of the MOPA system versus the BW of the OC-FBG.

Fig.4.8 shows the spectra of backward leakage lasers. In Fig.4.8, a valley at the emission wavelength 1080 nm emerges when the OC-FBG's BW becomes larger than 1.6 nm. The appearance of the valley results from the fact that the backward-propagation field at the HR-FBG end, $A^{-}(z = 0, t)$, has a BW larger than the HR-FBG's BW, so that part of the field is not bounded by the HR-FBG and thus strong backward leakage occurs.

Besides, as shown in Fig.4.9, the output spectra of the cavity are found to be broadened rapidly when the BW of OC-FBG increases from 0.3 nm to 1.6 nm, but the broadening effect becomes stagnant when the BW of OC-FBG reaches 1.6 nm.

Overall, the 1.6 nm OC-FBG is seemingly the tipping point in the MOPA simulations: it is linked to the saturation of SRS suppression, the boost of backward leakage power and the saturation of the seed laser broadening effect.

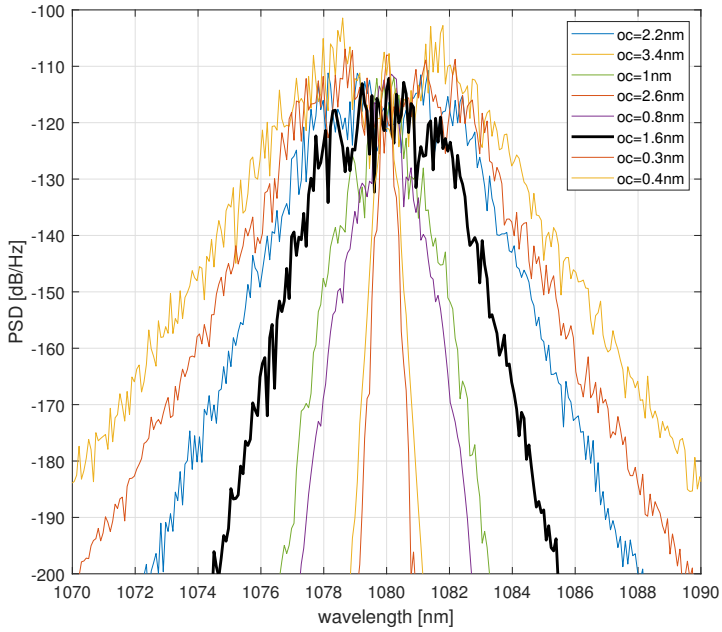

Figure 4.8: Simulation result: backward leakage PSDs of the MOPA system using different OC-FBGs.

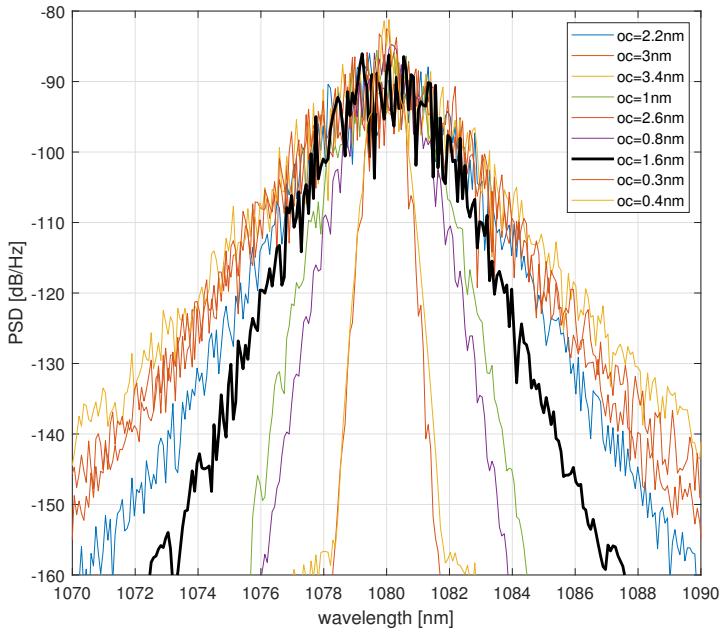

Figure 4.9: Simulation result: PSDs of seed lasers of the MOPA system using different OC-FBGs.

Two factors are found to have an impact on SRS in MOPA systems, including the power and BW of the seed laser [42, 41, 46]. In this simulation, OC-FBGs have little influence on the output power from the cavity, because the seed lasers' power are closed to each other. Thus the main factor that affects the SRS threshold in the MOPA simulations is the BW of the seed.

When the BW of OC-FBG goes beyond 1.6 nm, the seed laser stops broadening; the backward leakage power starts to boost; the SRS ratio stops to decrease. All these three phenomena are consistent and related to each other. Analysis below explains these linkages.

It is confirmed that a broader BW of the seed (given the same seed power) can suppress the SRS in the amplifier stage [42]. Thus, the SRS suppression effect saturates when the broadening effect on the seed stops.

In addition, the stagnant broadening of the seed can manifest itself in the boost of the leakage power from the HR-FBG end. The spectral profile of OC-FBG determines the BW of the initial condition for the backward propagation by Eqs.(3.9). The spectrum of backward-propagation field $A^-(z,t)$ becomes broadened during the backward propagation because of SPM. Thus, if the OC-FBG is broad enough, because of the SPM effect, the field at the HR-FBG end ($A^-(z=0,t)$) can be broader than the spectral profile of HR-FBG, leading to the boost of backward leakage power. Furthermore, once the strong backward leakage occurs, the BW of the initial condition for forward propagation ($A^+(z=0,t)$) is fixed to the BW of HR-FBG. In this case, after the forward propagation, the output spectrum is not broadened by a broader OC-FBG.

In summary, the broadening effect on the cavity output spectrum by broadening the OC-FBG saturates when the backward leakage power boosts, and thus the SRS suppression effect saturates accompanying with the saturation of the broadening of the cavity output laser.

In practice, it is ubiquitous to suppress SRS by the adoption of a broadband OC-FBG in a MOPA system. However, it is not trivial to decide the optimal BW of OC-FBG, especially in all-fiber configurations in which the cavity outputs (seed lasers) are difficult to detect. Based on the above simulations and discussion, for a given HR-FBG and given lengths of fibers, researchers and engineers should stop broadening the OC-FBG when the backward

leakage becomes strong. Or, in other words, researchers can always choose to broaden the OC-FBG when the backward leakage does not occur.

4.1.3 Summary

This section reports in detail the SRS suppression effect by broad OC-FBGs. It is found that the SRS suppression effect saturates when the BW of the OC-FBG increases beyond a point at which strong backward leakage power occurs. In addition, a suggestion to determine the choice of OC-FBG is given for experiments in practice.

4.2 Influence of OC-FBGs on fiber-oscillator systems

The influence of BWs of OC-FBGs on SRS threshold in single-oscillator configurations has been widely investigated experimentally and theoretically [20, 15]. In addition, the experiment in [39] investigated the impact from the shapes of OC-FBG's spectral profile on the SRS threshold. Spectral profiles of OC-FBGs were used and compared in single-oscillator HPFLs; the OC-FBGs' spectral profiles include narrow Gaussian, broad Gaussian, triangle and multi-peaks shapes. In [39], interestingly, the multi-peaks OC-FBG was capable of suppressing SRS as a broadband OC-FBG. In the meantime, the system using the multi-peaks OC-FBG had much smaller backward leakage power than the one using the broadband OC-FBG.

In this section, simulations are made to investigate the influence of different OC-FBGs on SRS threshold in single-oscillator HPFL systems.

4.2.1 Simulation plan

The simulated configuration is the co-pumping single-oscillator design shown in Fig.3.1. Parameters for the fiber oscillator simulation are listed in Tab.4.2. Pump power equal to 2500 W, pump wavelength equal to 976 nm and concentration $N_0 = 4 \times 10^{25}$ m^3 are chosen to guarantee the fully pump absorption. The nonlinear coefficient and dispersion coefficients are chosen as typical parameters for 20/400μm YDF [41].

Table 4.2: Parameters for the YDF in the single-oscillator simulation

Parameter	Value	Parameter	Value
λ_p	976 nm	λ_s	1080 nm
Γ_p	0.0037	τ	0.85 ms
N_0	$4 \times 10^{25}\mathrm{m}^{-3}$	L	20 m
γ	5 $\mathrm{W}^{-1}/\mathrm{km}$	Γ_s	0.85
β_2	20.4 $\mathrm{ps}^2/\mathrm{km}$	β_3	0.04 $\mathrm{ps}^3/\mathrm{km}$

The simulated HR-FBG has a super-Gaussian spectral profile with 4 nm FWHM and 99.5% maximum reflectivity. Various OC-FBGs are used in simulations, including super-Gaussian shape FBGs with BW from 0.2 nm to 3 nm and CM-FBG. CM-FBGs are represented by multi-peak spectral profiles, which are shown in Fig.4.10. Each CM-FBG constitutes five 0.2-nm super-Gaussian peaks and has an envelope identical to the spectral profile of 3 nm OC-FBG. By tuning the interval between peaks, a dense-distributed multi-peak profile and a sparse one are made for comparison.

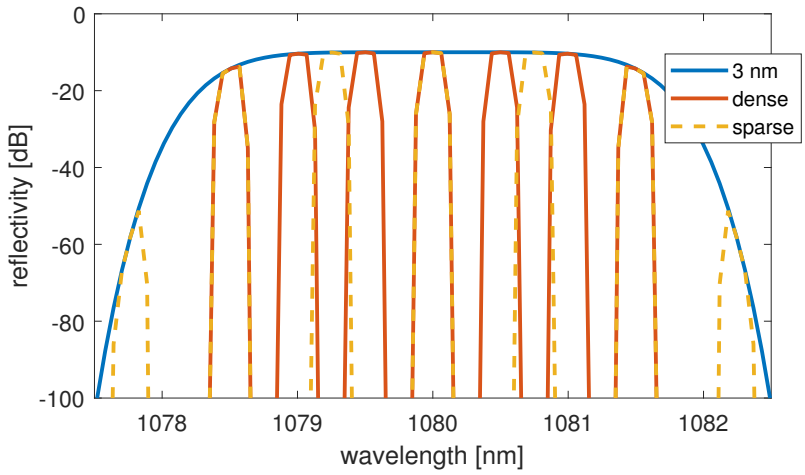

Figure 4.10: Spectral profiles of the 3 nm super-Gaussian shape OC-FBG (blue line), dense-distributed CM-FBG (red line), and sparse-distributed CM-FBG (yellow dotted line).

Compared to the short cavity used in the MOPA simulation, the variation of outputs are stronger for fiber-oscillator simulations. Thus, 50 iterations are recorded for post-processing to assure the reproducibility of the simulation results.

4.2.2 Simulation results and discussion

Simulation results of super-Gaussian OC-FBGs

To demonstrate the evolution of optical powers and excitation ratio along the fiber in the simulations, the simulation result of 0.2 nm OC-FBG is shown in Fig.4.11. In this figure, the excitation ratio N_2/N_0 drops from about 17.8% to about 2.3%; the pump power P_p is depleted from 2200 W to 30 W; the backward-propagation power P^- is amplified from about 10 W to about 180 W; the forward-propagation power P^+ increases from 180 W to about 1995 W during the forward propagation process. The gain for P^+ becomes saturated because the N_2/N_0 is becoming small along the fiber.

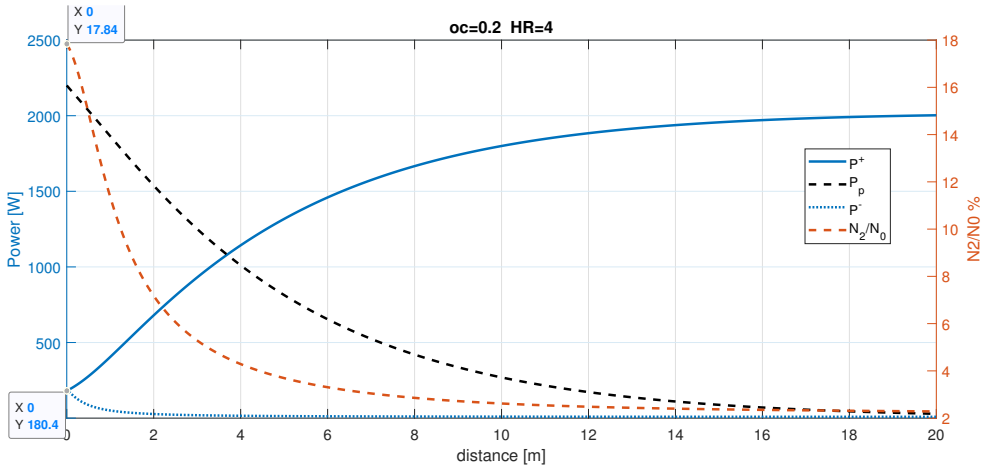

Figure 4.11: Power versus distance when 0.2 nm OC-FBG is used. $P^+(z=0)$ and $\frac{N_2}{N_0}|_{z=0}$ are highlighted.

Fig.4.12 shows the SRS ratios of the averaged output spectra as a function of the BWs of OC-FBGs. The SRS ratio drops basically from -14.5 dB to -25.5 dB when the BW of the OC-FBG increases from 0.2 nm to 3 nm. The SRS ratio is mitigated hugely when the OC-FBG is broadened from 0.2 nm to 0.6 nm, but the SRS suppression effect becomes insignificant when the OC-FBG is broader than 1 nm.

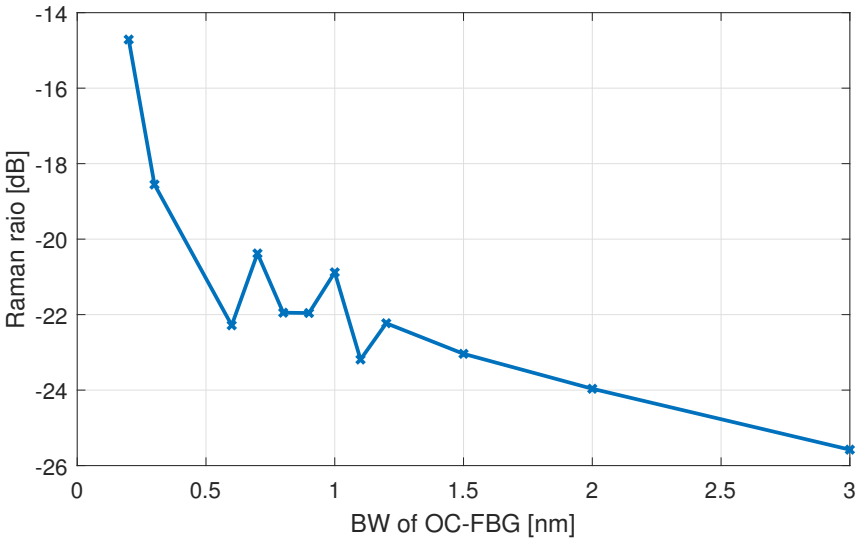

Figure 4.12: SRS ratio as a function of the BW of the OC-FBG.

Fig.4.13 shows the output spectra of the OC-FBGs with 0.2 nm and 3 nm BW. As expected, with the rise of OC-FBG's BW, the linewidth at the emission wavelength 1080 nm is increasingly broadened, and the peak of SRS Stokes (1134 nm) is correspondingly mitigated.

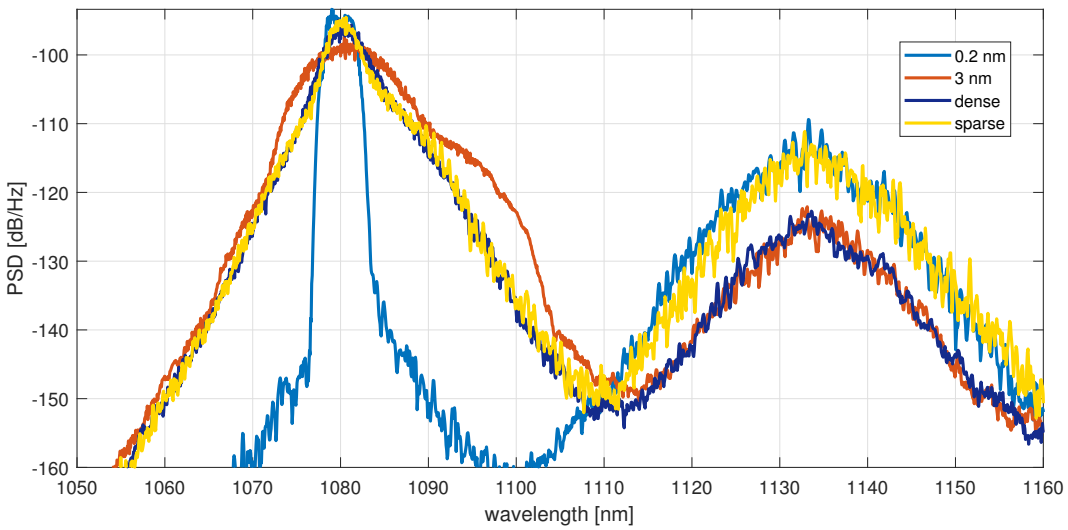

Figure 4.13: Output spectra for 0.2 nm, 3 nm OC-FBGs as well as dense and sparse CM-FBGs.

The output powers for each OC-FBG are shown in Fig.4.14. Despite some fluctuations,

a decreasing trend of output power can be observed when the OC-FBG is becoming broader. The output power drops from about 1995 W to about 1890 W when the OC-FBG's BW rises from 0.2 nm to 3 nm. This trend agrees with the simulation result in [20] and the experimental result in [39]. The fluctuations in Fig.4.14 and Fig.4.12 result from numerical artefacts. [20] showed that the output of this iterative oscillator model varies from iteration to iteration, and the variance of outputs over iterations becomes larger when a narrow OC-FBG is adopted in the simulation. More stable and reproducible outputs can be made by using a larger averaging number [20], but this boosts the time consumption of the computation at the same time.

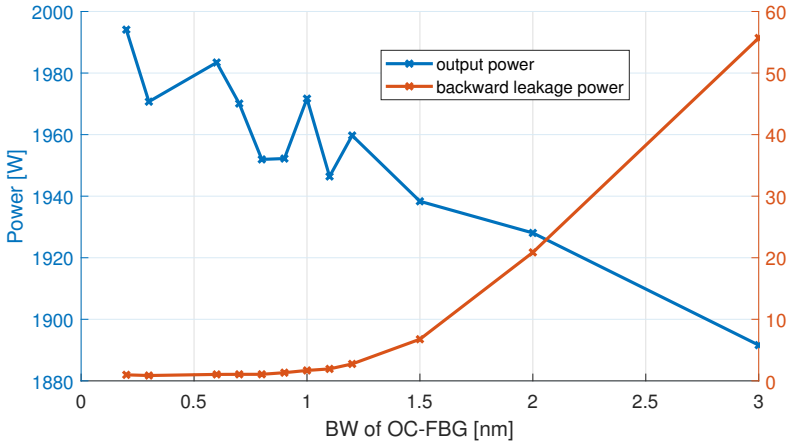

Figure 4.14: Output power and backward leakage power of different BW of the OC-FBG.

For each OC-FBG, 50 iterations after the output power converges are recorded for post-processing. Fig.4.15 shows the output powers of recorded iterations in the case of the 0.2 nm OC-FBG and 3 nm OC-FBG. The narrower OC-FBG's power output varies more significantly, and has a stronger power in average, compared to a broader OC-FBG. Fig.4.16 shows the SRS ratio varies over iterations for different OC-FBGs. This figure shares the same trends in [20] that a narrower OC-FBG's SRS ratio outputs are more significantly fluctuating; a larger SRS ratio of the output spectrum is more probable to occur.

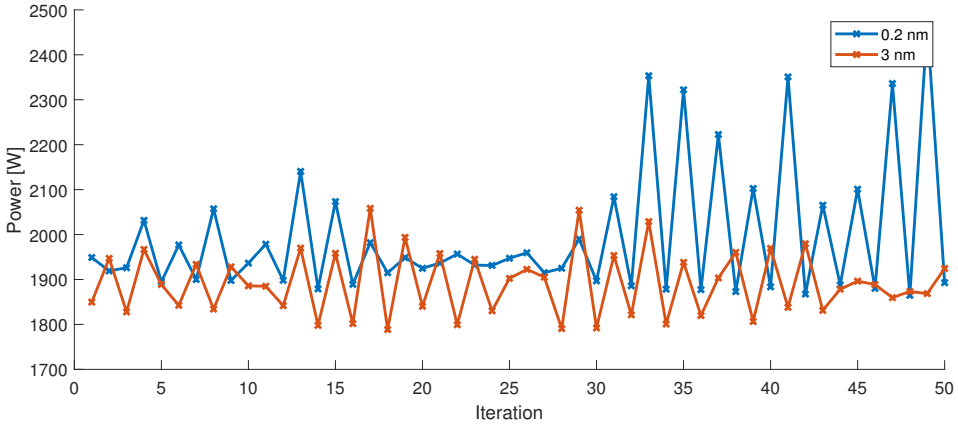

Figure 4.15: Output power as a function of iterations for 0.2 nm and 3 nm OC-FBGs.

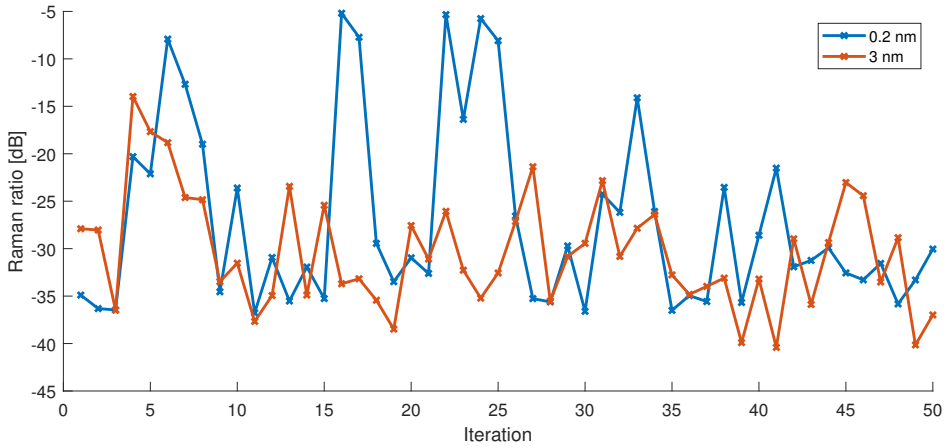

Figure 4.16: SRS ratio as a function of iterations for 0.2 nm and 3 nm OC-FBGs.

The backward leakage power has shown its importance in analysis of SRS threshold in the previous section. The dependence of backward leakage power on the BW of OC-FBG is plotted in Fig.4.14. From the figure, the backward leakage power keeps stable around 1 W at the beginning, and boosts exponentially when the OC-FBG's BW is larger than 1 nm. The explanation for this boost is identical with the one in the previous section, in which the backward propagating light A^- is broadened during the backward propagation process and finally its BW is broader than HR-FBG. Fig.4.17 shows the spectra of backward leakage light of various OC-FBGs. With the rise of the BW of OC-FBG, the backward leakage spectrum gradually evolves from a spike shape to a valley shape. In addition, for the valley-shape backward leakage spectra in the case of 2 nm or 3nm OC-FBG, the lobe

at the longer wavelength is larger than the lobe at the shorter wavelength. This simulation phenomenon agrees with the experimental results in [43]. The reason leads to the asymmetric backward leakage spectra is that the asymmetric gain spectral profiles, which is demonstrated in Fig.4.18, have stronger amplification capacity on longer wavelengths when the excitation ratio N_2/N_0 is just a few percent.

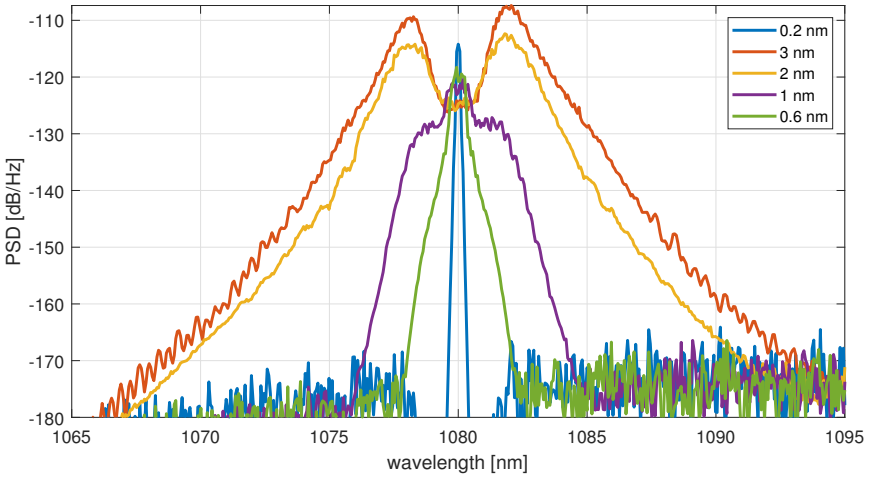

Figure 4.17: Backward leakage spectra for OC-FBGs with the BW of 0.2 , 0.6 nm, 1 nm, 2 nm and 3 nm.

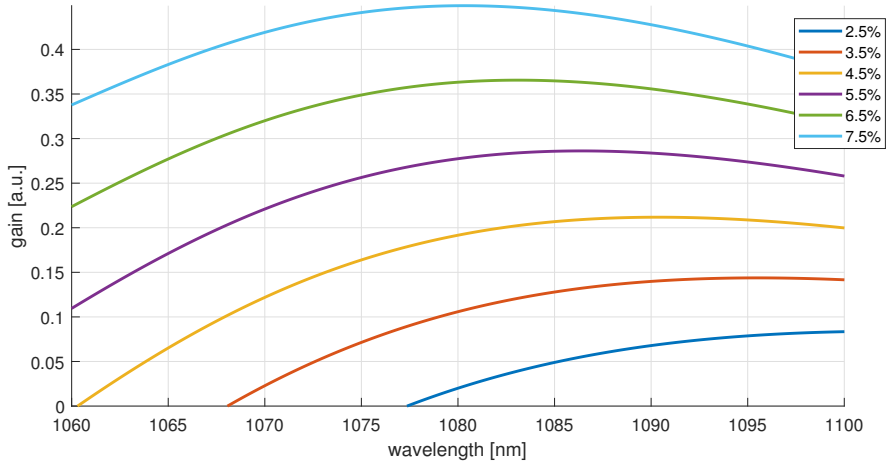

Figure 4.18: Yb-gain profiles for excitation ratios N_2/N_0 ranging from 2.5% to 7.5%.

When the strong backward leakage occurs (OC-FBG $>$ 1 nm), the initial conditions for forward propagating fields $A^+(z=0,t)$ have the same spectral profile identical to the spectral

profile of HR-FBG. But $A^+(z=0,t)$ for different OC-FBGs have different power. Thus, it is interesting to analyse the details in the simulation results of broadband OC-FBGs.

Fig.4.19 to Fig.4.21 show the power evolution and the excitation ratio along the fiber for 1.5 nm, 2 nm and 3 nm OC-FBGs, respectively. In comparison of these results, a broader OC-FBG has a larger power of $A^+(z=0,t)$; N_2/N_0 at the beginning of the fiber has a higher value for a broader OC-FBG. These results show that a broad OC-FBG leads to a smaller gain for the forward propagation, which might mitigate the SRS effect in the forward-propagation process.

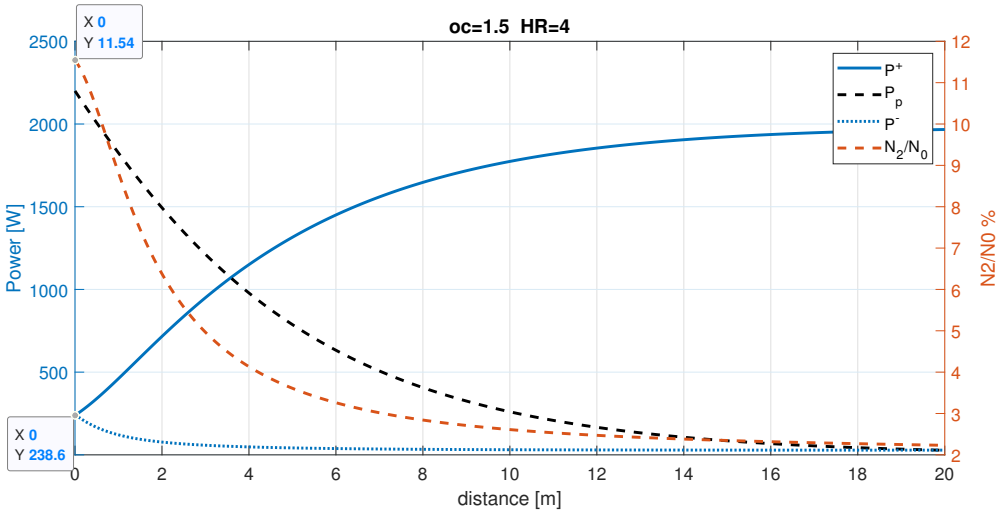

Figure 4.19: Power versus distance and excitation ratio versus distance for 1.5 nm OC-FBG. $P^+(z=0)$ and $\frac{N_2}{N_0}|_{z=0}$ are highlighted.

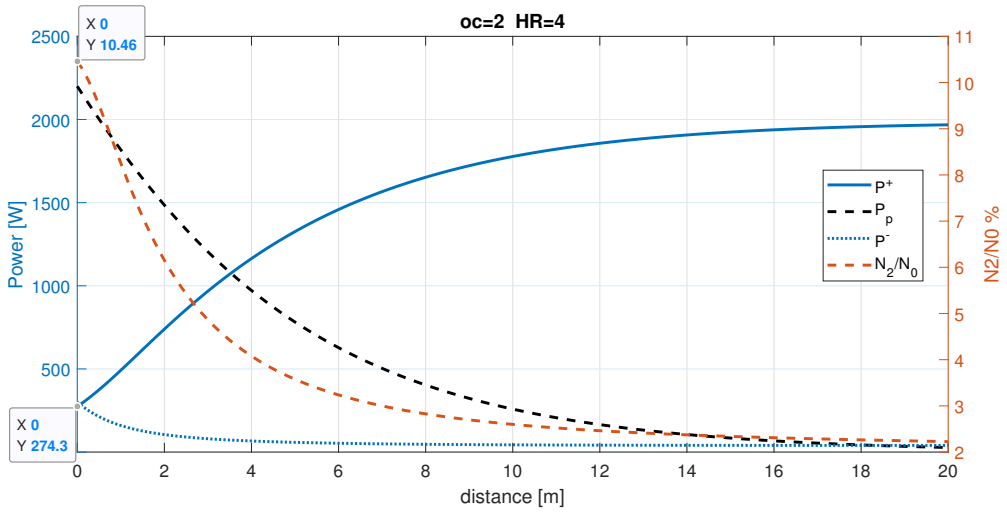

Figure 4.20: Power versus distance and excitation ratio versus distance for 2 nm OC-FBG. $P^{+}(z=0)$ and $\frac{N_2}{N_0}|_{z=0}$ are highlighted.

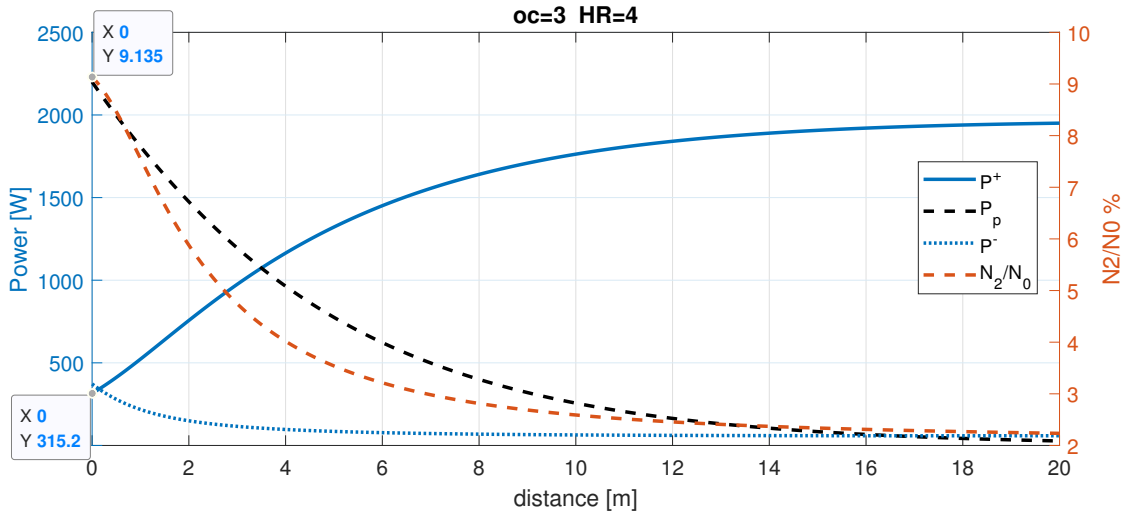

Figure 4.21: Power versus distance and excitation ratio versus distance for 3 nm OC-FBG. $P^{+}(z=0)$ and $\frac{N_2}{N_0}|_{z=0}$ are highlighted.

Simulation results of CM-FBGs

Tab.4.3 compares the main performance of narrowband OC-FBG, broadband OC-FBG, sparse CM-FBG and dense CM-FBG in simulations. Even though with the same envelope of spectral profile as the broad OC-FBG, CM-FBGs' backward leakage powers are hugely mitigated compared to the broad OC-FBG, as the backward leakage power drops from 3 nm OC-FBG's 55.7 W to CM-FBGs' around 15 W. By changing the 3 nm OC-FBG to a

CM-FBG (dense or sparse type), the output power is improved and approaches the narrow OC-FBG's output power. In terms of the performance in the SRS ratio, the dense CM-FBG is able to suppress SRS as good as the broad OC-FBG, whereas the sparse CM-FBG has -15.7 dB SRS ratio, which is similar with the narrow OC-FBG's -14.7 dB SRS ratio.

Table 4.3: Comparison between various OC-FBGs

	SRS ratio [dB]	Output power [W]	backward leakage power[W]
0.2nm	-14.7	1994	0.988
sparse	-15.7	1993	14.3
dense	-25.8	1937	15.7
3nm	-25.6	1892	55.7

The simulation results agrees with the experimental results in [39]: in comparison with the broad OC-FBG, a CM-FBG with the same spectral envelope has a similar Raman suppression, while it has a lower value of backward leakage power and a better conversion efficiency. When the shape of the CM-FBG changes from dense to sparse, the CM-FBG's performance approaches the narrowband OC-FBG's, leading to a higher output power, smaller backward leakage power and a higher SRS ratio. Some detailed simulation results are presented in the rest of this section.

Fig.4.13 compares the output spectra of the dense CM-FBG, sparse CM-FBG, 0.2 nm narrow OC-FBG and 3 nm flat-top OC-FBG. The dense CM-FBG has the same SRS suppression capacity as the 3 nm OC-FBG does, in which the SRS ratio is mitigated to around -26 dB. The SRS ratio of sparse CM-FBG is -15.7 dB, which is close to the one of 0.2 nm OC-FBG. The linewidths of emission wavelength (1080 nm) for CM-FBGs' output spectra are narrower than 3 nm OC-FBG's.

The backward leakage spectra of CM-FBGs are shown in Fig.4.22. The backward leakage spectra of dense and sparse CM-FBG have similar envelopes, and they are both smaller than the spectrum of 3 nm OC-FBG. In addition, for the sparse CM-FBG, there are more ripples in the backward leakage spectrum in comparison with the dense CM-FBG.

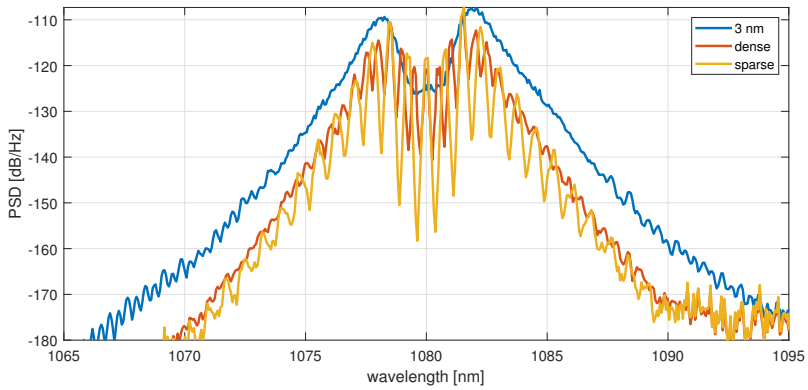

Figure 4.22: Backward leakage spectra for 3 nm OC-FBG, dense CM-FBG and sparse CM-FBG.

Fig.4.23 and Fig.4.24 shows optical powers and excitation ratio along the fiber for the dense CM-FBG and the sparse one, respectively. Compared to the 3 nm OC-FBG shown in Fig.4.21, the backward-propagation power $P^{-}(z)$ of CM-FBGs is decreased; the excitation ratio N_2/N_0 at $z = 0$ is decreased; the forward-propagation power at the end of the fiber $P^{+}(z = 20)$ is increased.

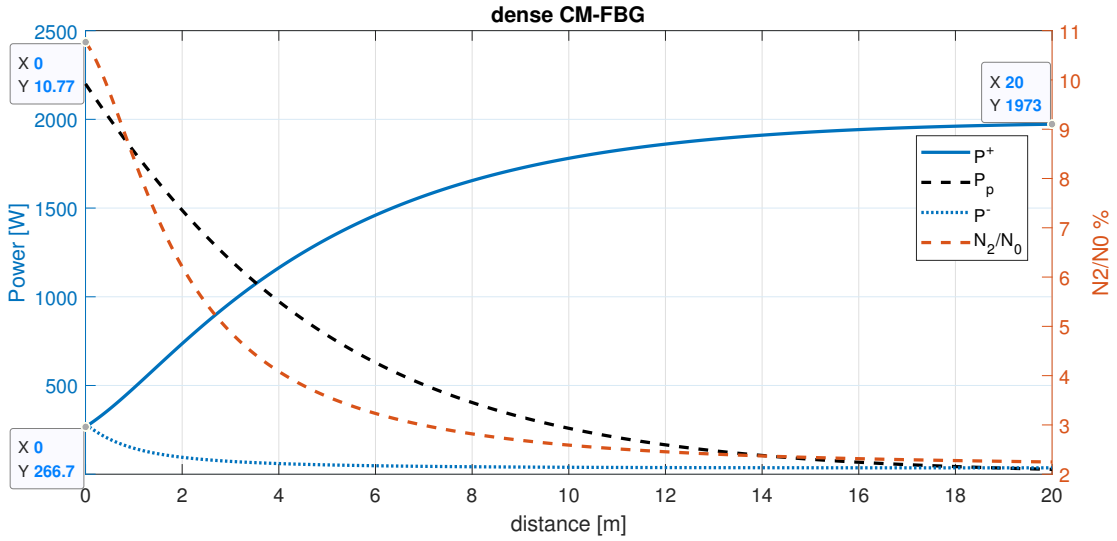

Figure 4.23: Power versus distance and excitation ratio versus distance for dense CM-FBG. $P^{+}(z = 0)$, $P^{+}(z = 20)$ and $\frac{N_2}{N_0}|_{z=0}$ are highlighted.

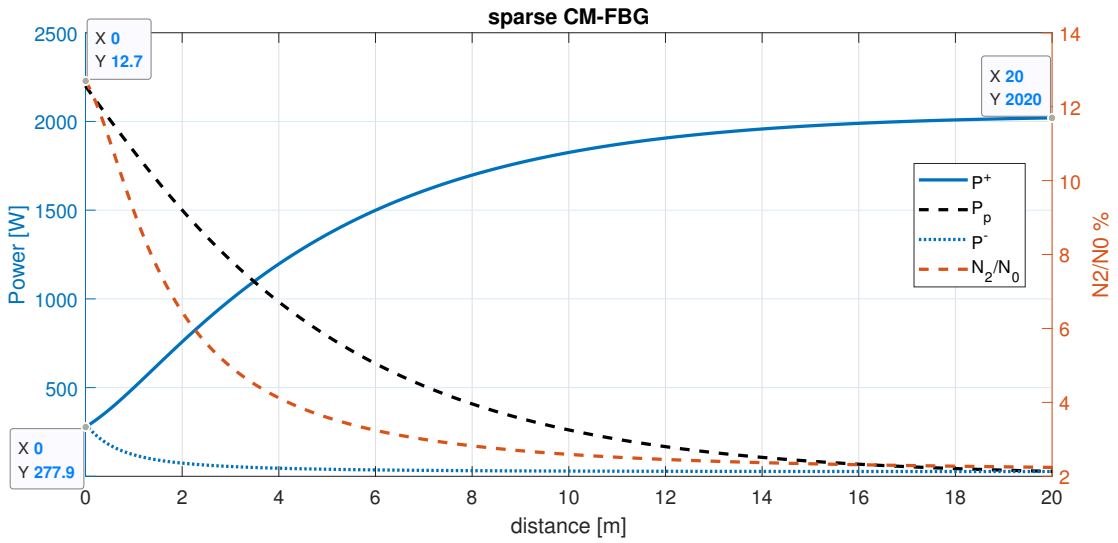

Figure 4.24: Power versus distance and excitation ratio versus distance for sparse CM-FBG. $P^+(z=0)$, $P^+(z=20)$ and $\frac{N_2}{N_0}|_{z=0}$ are highlighted.

4.2.3 Summary

In this section, 20-meter Yb-doped fiber oscillators with various OC-FBGs are simulated by using the NLSE-based oscillator model.

For a super-Gaussian-shape OC-FBG with a larger BW, the output power is reduced; the SRS ratio is mitigated; and the backward leakage power is increased. All these simulation results match the experimental results in studies [15, 39]. In addition, the simulation outputs of this oscillator model over iterations are analysed in detail, since the outputs of this model vary from iteration to iteration. The level of the variation is related to the BW of the simulated OC-FBG: a narrower OC-FBG is more probable to generate a output with larger power and larger SRS ratio. Because of the variation of outputs, a number of outputs have to be recorded for post-processing in order to guarantee stable and reproducible simulation results.

The experimental results of the influence of the CM-FBG in study [39] has been successfully simulated by the NLSE-based fiber-oscillator model. In the simulation results, compared to a broadband OC-FBG, a CM-FBG (represented by a multi-peak spectral profile) with a same spectral envelope has a same capacity to suppress SRS. In addition, the distribution of the peaks in the spectral profile of a CM-FBG has impact on the performance:

a sparse-distributed-peak spectral profile of CM-FBG leads to performances similar to the performances of a narrowband OC-FBG; a denser-distributed CM-FBG has a same SRS suppression capacity as a broadband OC-FBG (with the same spectral envelope), while the backward leakage power is largely mitigated for CM-FBGs.

4.3 Conclusion

In this chapter, simulations of MOPA systems and fiber-oscillator systems were successfully simulated by using NLSE-based models. The influence of OC-FBGs on the performance of HPFL systems was reported.

For a co-pumping MOPA system, a OC-FBG can influence the SRS threshold by governing the BW of the seed laser. A broad OC-FBG can broaden the spectrum of the seed laser and thus suppress the SRS. In addition, the backward leakage power from the HR-FBG was found to reveal the information of the saturation of SRS suppression effect by broadening the OC-FBG.

For simulations of fiber-oscillators, stable and reproducible outputs were done by averaging a large number of outputs. The broadened OC-FBG's SRS suppression effect was successfully simulated. In addition, the experimental results [39] of CM-FBGs were successfully simulated by the NLSE-based oscillator model.

In the simulation results, OC-FBGs influence the fiber-oscillator systems from multiple aspects, including the power of backward-propagation field, the initial condition of forward-propagation field, as well as the excitation ratio along the fiber; compared to the broadband OC-FBG, the CM-FBG with the same spectral envelope has comparable capacity of suppressing SRS effect, lower backward leakage power and better conversion efficiency. These simulation results matched the experimental results in study [39]. To the best of our knowledge, this is the first work to theoretically investigate the CM-FBG in fiber-oscillators.

The simulation results of this chapter proved that NLSE-based models is capable of simulating CW-HPFL systems. The detailed simulation results of various OC-FBGs in this chapter revealed a better understanding for OC-FBGs' impact on CW-HPFLs.

Chapter 5

Simulation of IM-FWM in LMA CW-amplifiers

This chapter focuses on intermodal couplings between FM and HOM in CW-HPFLs. A model based on MM-GNLSEs is developed and used to simulate the intermodal couplings in 25/400 μm Yb-doped amplifiers. A method to simulate the degenerate IM-FWM is given in this chapter. By using this model, a novel phenomenon is found, which results from the joint effect of IM-FWM [47] and SRS-induced IM-WM [48].

5.1 Introduction of IM-FWM and SRS-induced IM-WM in a multi-mode fiber

Researchers have recently started to focus on the coupling between FM and HOM when analyzing the nonlinear effects in CW high-power amplifiers. Liu [48] applied MM-GNLSE into simulating LMA amplifiers containing LP_{01} and LP_{11} modes; Liu pointed out, theoretically, that SRS-induced IM-WM can transfer power from the emission wavelength of FM to the SRS Stokes light of HOM. Compared to the intra-modal Raman effect and Raman amplification of FM, this IM-WM effect is dominant in generating Raman-Stokes of HOM in two-mode amplifiers. The equations depicting these terms are given in the coming sections.

For a better illustration of the phenomenon of SRS-induced IM-WM, Fig.5.1 shows a

simulation result of SRS-induced IM-WM. By amplifying a purely FM seed in a two-mode amplifier (the initial condition of HOM is set as white noise), the output spectra of modes are shown in Fig.5.1, where HOM is only generated around the wavelength of Raman-Stokes 1134 nm. In this case, SRS-induced IM-WM dominates the mode coupling process; the power is transferred from FM emission wavelength (1080 nm in LP_{01}) to SRS Stokes light in HOM (1134 nm in LP_{11}).

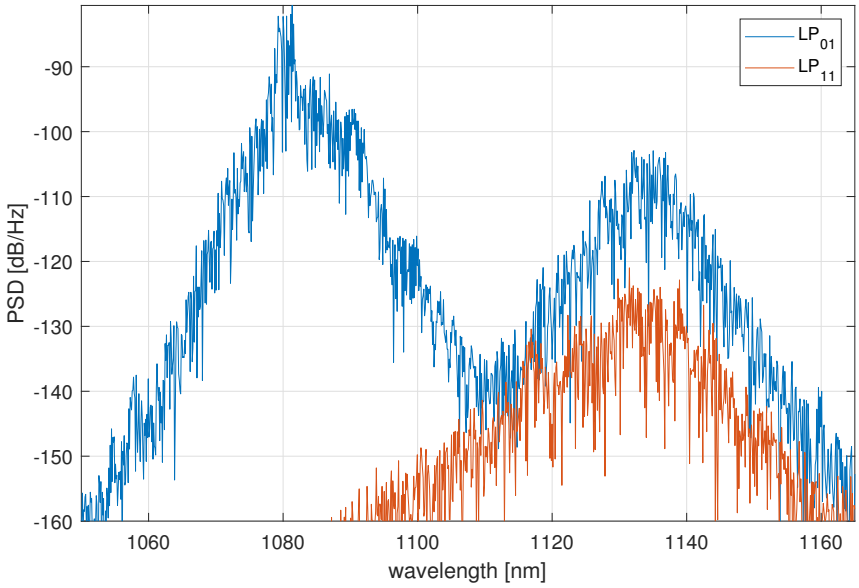

Figure 5.1: Simulation result for illustrating SRS-induced IM-WM.

Furthermore, Yin [47] theoretically and experimentally demonstrated that IM-FWM exists in MOPA systems using LMA fibers such as 20/400 or 25/400 μm YDFs. Especially, in typical commercial 25/400 μm YDFs, degenerate IM-FWM between LP_{01} and LP_{11} is the dominant intermodal parametric process; this phenomenon generates Stokes at LP_{11} and idler at LP_{01}. In [47], by choosing a proper bend-radius of a LMA fiber, the Stokes and idler from IM-FWM can be erased because HOM content in the fiber is suppressed. This experiment further proved the existence of IM-FWM in LMA YDFs.

To illustrate the phenomenon of degenerate IM-FWM in high-power fiber amplifiers, Fig.5.2 shows a simulation result of degenerate IM-FWM between LP_{01} and LP_{11} in 25/400 μm YDF. Degenerate IM-FWM can be explained that two photons in different modes (LP_{01} and LP_{11}) at the same wavelength (1080 nm) produce Stokes (1057 nm) in LP_{01} and idler

(1103 nm) in LP_{11}, as shown in Fig.5.2.

For degenerate IM-FWM in LMA fibers, because the contribution from nonlinear effects is negligible in the phase-matching condition, the phase-matching condition is satisfied by the contribution from material dispersion and waveguide dispersion [47]. Thus, when using MM-GNLSE to simulate IM-FWM, the chosen $\beta_n^{(01,11)}$ (the n^{th} order derivative of the propagation constant of LP_{01} or LP_{11}) is important to generate the expected pair of Stokes and idler. A proper way to choose $\beta_n^{(01,11)}$ is given and discussed in the theory section.

A model based on MM-GNLSE is introduced and explained in Sec.5.2; an IM-FWM simulation for 25/400 μm YDF is done and discussed in Sec.5.3; the conclusion is drawn in the last section.

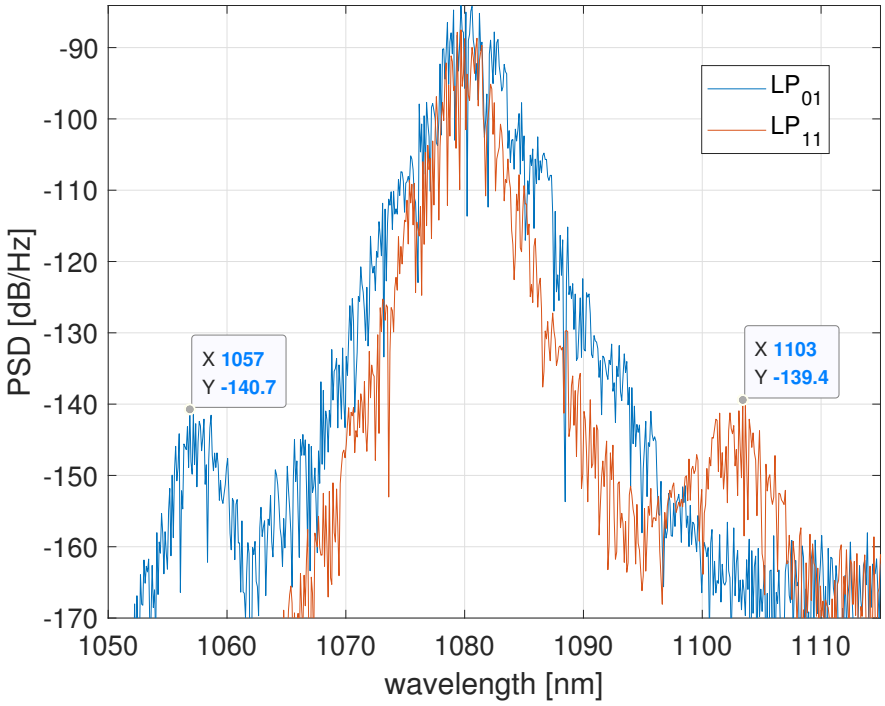

Figure 5.2: Simulation result for illustrating degenerate IM-FWM between LP_{01} and LP_{11} in 25/400 μm YDFs. Stokes at 1103 nm in HOM and idler at 1057 nm in FM are highlighted.

5.2 Introduction of model based on MM-GNLSE for simulating 25/400 μm YDF

Different from the conventional CW-laser modeling using power-balance-equations [5, 13, 18], researchers began to regard HPFLs as quasi-CW systems and simulate them with NLSE [41, 42, 15]. However, the simulations in [41, 42, 15] were solely based on single-mode NLSEs; the HOM content was not considered in these studies. Recently, Liu [48] used MM-GNLSE to simulate the interaction between LP_{01} and LP_{11} modes in LMA fiber amplifiers. Thus, by extending the work in the study[48], more features regarding intermodal-couplings in high-power amplifiers can be revealed.

Based on [48], the MM-GNLSE for an amplifier can be written in the form as $\partial_z A_u(z,t) = D^{(u)}(z,t) + N^{(u)}(z,t) + G^{(u)}(z,t)$, which considers the effects of dispersion, nonlinearity and Yb-ion gain, respectively. In this section, the principle of MM-GNLSE is presented and these three terms on the right hand side are explained. The method to choose a proper differential group velocity between modes is investigated in order to simulate the desired frequency-shift of degenerate IM-FWM.

5.2.1 Principle of MM-GNLSE in passive fibers

Deriving from Maxwell equations, Poletti gave the following MM-GNLSE for mode p [49]. By neglecting the shock time constant and a fast-rotating term in the convolution and considering only two modes in the fiber, the MM-GNLSE in [49] can be written as follow:

$$\partial_z A_p(z,t) = D^{(p)}(z,t) + N^{(p)}(z,t) \tag{5.1}$$

where A_p is the complex amplitude of mode p; $D^{(p)}$ is the dispersion term of mode p; $N^{(p)}$ is the nonlinearity term of mode p.

$$D^{(p)}(z,t) = i(\beta_0^{(p)} - \beta_0)A_p(z,t) - (\beta_1^{(p)} - \beta_1)\partial_t A_p(z,t) + i\sum_{n\geq 2}\frac{\beta_n}{n!}(i\partial_t)^n A_p(z,t) \tag{5.2}$$

where $\beta_n^{(p)}$ is the n^{th} order derivative of propagation constant of mode p; constants β_0 and $1/\beta_1$ are free parameters regarding to an overall phase factor and the velocity of a reference frame [49].

$$N^{(p)}(z,t) = i\gamma \sum_{l,m,n} \{f_{plmn} A_l(z,t) \int d\tau R(\tau) A_m(z,t-\tau) A_n^*(z,t-\tau)\} \tag{5.3}$$

$p,l,m,n = 1$ or 2 representing the FM or HOM; $R(\tau) = (1-f_R)\delta(t) + f_R h(t)$, where $f_R = 0.18$ is fractional contribution of the Raman response to the total nonlinearity and $h(t)$ is the delayed Raman response function for silicon [5]; $\gamma = \frac{n_2\omega_0}{cA_{eff,1111}}$ is the nonlinear Kerr coefficient of FM [5]; normalized overlap integral $f_{plmn} = Q_{plmn}/Q_{1111}$, and Q_{plmn} is overlap integral defined as

$$\begin{aligned} Q_{plmn} &= \frac{\int \vec{E}_p^* \vec{E}_l \vec{E}_m \vec{E}_n^* d\sigma}{N_p N_l N_m N_n} \\ N_p &= (\int (\vec{E}_p)^2 d\sigma)^{1/2} \end{aligned} \tag{5.4}$$

In Eqs(5.4), the field of mode p can be expressed as $\vec{E}_p(r,\phi) = \vec{E}_p(r)\exp(im_p\phi)$ in step-index fibers; $\vec{E}_p(r)$ is a symmetric mode profile with polarization, $\exp(im_p\phi)$ is an angular term, m_p is an integer. To achieve a non-zero Q_{plmn}, selection rules must be satisfied in terms of polarizations and angular parts[49]. Thus, following the analysis in [50, 49, 51], all overlap integrals containing subscripts with 3 LP_{01} modes or 3 LP_{11} modes are considered to be zeros, such as Q_{1112}, Q_{1222} and so forth.

5.2.2 Parametric process in MM-GNLSEs and Phase-matching condition

The same notation in [47] is adopted to describe the types of parametric processes. For instance, (11,01→11,01) refers to the parametric process that LP_{11} and LP_{01} modes both at the emission wavelength generate Stokes in LP_{11} and idler in LP_{01}. For the parametric

processes with 2 LP_{11} modes, we start to analyze with (11,01→11,01), which is the most possible IM-FWM occurring in 25/400 μm YDFs [47].

The nonlinear phase contribution is neglected in the analysis of IM-FWM [47]. Thus, the phase-matching condition of (11,01→11,01) is represented as

$$\beta^{(11)}(\omega_0) + \beta^{(01)}(\omega_0) = \beta^{(11)}(\omega_0 - \Delta\omega) + \beta^{(11)}(\omega_0 + \Delta\omega) \tag{5.5}$$

where $\beta^{(11)}(\omega_0)$ is the propagation constant of LP_{11} mode at central wavelength, $\beta^{(11)}(\omega_0 - \Delta\omega)$ is the the propagation constant of LP_{11} mode at Stokes wavelength, and so forth.

By applying Taylor expansion to the third order on both sides of Eqs(5.5), after some simple algebra, the phase-matching frequency shift $\Delta\nu$ is derived to be

$$\Delta\nu = \Delta\omega/(2\pi) = \frac{\beta_1^{(11)} - \beta_1^{(01)}}{\pi(\beta_2^{(11)} + \beta_2^{(01)})} \tag{5.6}$$

where $\Delta\nu$ is the degenerate IM-FWM frequency shift , β_1 is group velocity, β_2 is dispersion.

$\Delta\nu$ of this kind of parameter process should exist stably because it is independent of $\beta_0^{(01,11)}$, because $\beta_0^{(01,11)}$ is highly sensitive to the change of environment such as bending of fibers and temperature [51].

For the phase-matching condition of (11,11→01,01) or (01,01→11,11), using the same Taylor expansion method, $\Delta\nu$ of these kinds are found to depend on $\beta_0^{(01,11)}$. Experiment in [51] agrees that this kind of β_0-dependent parametric processes are not stable and not observable. Thus (11,11→01,01) or (01,01→11,11) will be neglected in the following simulation, which means Q_{1221} and Q_{2112} in Eqs(5.4) are set as zero.

To represent the degenerate IM-FWM of (11,01→11,01), the terms of intermodal cross-phase-modulation (IM-XPM) are used [50]. Therefore, by assuming that LP_{01} and LP_{11} are co-polarized for convenience, the final model in this paper is as same as the equations used in [48]. In addition, the spontaneous-emission noise term is neglected in order to speed up the computation.

5.2.3 Rate-equation and pump-depletion equation

To express the evolution of net gain in two-mode fibers, the net gain term, $G^{(u)}(z,t)$, in [48] is used, where the net gain Eqs(5.7) is governed by pump-depletion equation Eqs(5.8) and the excitation ratio Eqs(5.9).

Net gain term:

$$G_u(z,\omega) = \frac{1}{2}\{[(\sigma_a(\omega)+\sigma_e(\omega))N_2(z) - \sigma_a(\omega)N_0]\Gamma_u - \alpha_u\}A_u(z,\omega) \tag{5.7}$$

Pump depletion equation:

$$\frac{d}{dz}P_p(z) = -\Gamma_p\{\sigma_a(\omega_p)N_0 - (\sigma_a(\omega_p)+\sigma_s(\omega_p))N_2(z)\} - \alpha_p P_p(z) \tag{5.8}$$

Excitation ratio:

$$\frac{N_2}{N_0} = \frac{\frac{\Gamma_p}{\hbar\omega_p A}\sigma_a(\omega_p)P_p + \frac{1}{2\pi T_m A}\int \frac{\sigma_a(\omega)}{\hbar\omega}(\Gamma_u|A_u(z,\omega)|^2 + \Gamma_v|A_\nu(z,\omega)|^2)d\omega}{\frac{\Gamma_p}{\hbar\omega_p A}(\sigma_a(\omega_p)+\sigma_s(\omega_p))P_p + 1/\tau + \frac{1}{2\pi T_m A}\int \frac{\sigma_a(\omega)+\sigma_s(\omega)}{\hbar\omega}(\Gamma_u|A_u(z,\omega)|^2 + \Gamma_v|A_\nu(z,\omega)|^2)d\omega} \tag{5.9}$$

In Eqs(5.7 to 5.9), subscripts u and ν refers to either LP_{01} or LP_{11} mode in the core; subscript p refers to the pump wavelength; σ_a and σ_e are absorption and emission cross sections, respectively; Γ is the power overlap factor between transverse modes and dopant area; N_0 is the dopant concentration of the active gain medium; N_2/N_0 is the excitation ratio; A is the doped-cress section area; T_m is the time window used in the calculation; $\hbar$ is the Planck's constant; α is the loss coefficient; τ is the life of the excited Yb-ions.

5.2.4 Summary for the simulation model

To sum up, after the above introduction, in MM-GNLSE $\partial_z A_u(z,t) = D^{(u)}(z,t) + N^{(u)}(z,t) + G^{(u)}(z,t)$, the dispersion term $D^{(u)}(z,t)$ can be expressed as Eqs(5.2); the net gain term $G^{(u)}(z,t)$ is calculated by Eqs(5.7 to 5.9); the nonlinear term in two-mode fibers $N^{(u)}(z,t)$

can be written as

$$N^{(u)}(z,t) = i\gamma\{Q_{uu}A_u(z,t)\cdot R(t)\otimes|A_u(z,t)|^2 + Q_{u\nu}A_u(z,t)\cdot R(t)\otimes|A_\nu(z,t)|^2 + Q_{u\nu}A_u(z,t)\cdot R(t)\otimes[A_\nu^*(z,t)A_u(z,t)]\} \tag{5.10}$$

where subscript u or ν refers to either FM or HOM, Q is the normalized integral, $R(t) = (1-f_R)\delta(t) + f_R h(t)$ and $\otimes$ denotes convolution operation. For the nonlinear term in Eqs(5.10), the first term on the RHS represents SPM and intre-modal Raman scattering, the second term represents intermodal XPM and Raman amplification from the other mode, and the last term depicts intermodal XPM and SRS-induced IM-WM.

Besides, split-step Fourier Method [5] is used in the computation.

5.3 Simulation

5.3.1 Simulation scheme

Fig.5.3 demonstrates the simulation scheme of a co-pumping MOPA system, including a multi-mode seed laser, LD pumping sources and a two-mode YDF.

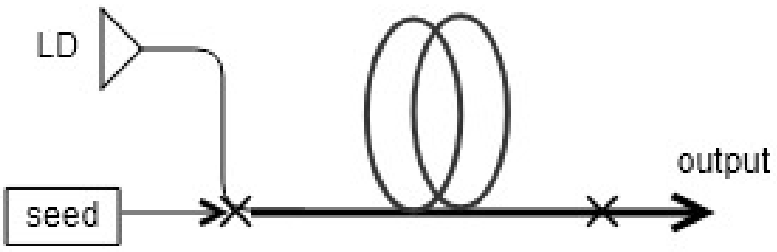

Figure 5.3: Schematic of simulation for a multi-mode co-pumping fiber amplifier. A multi-mode seed laser is injected into a two-mode amplifier, which is pumped by LD sources.

The HOM content in the seed laser is introduced by

$$A_{FM} = A_{SM}\sqrt{(1-H)} \tag{5.11}$$

$$A_{HOM} = A_{SM}\sqrt{H} \tag{5.12}$$

where A_{SM} is the complex amplitude of a single-mode output generated from the single-mode oscillator model in [41]; H is the assumed HOM content percentage in the seed laser; A_{FM} is the complex amplitude of fundamental-mode in the seed; A_{HOM} is the HOM content.

In terms of the single-mode oscillator model, the same model in [41] is used, which is a boundary condition model with boundaries represented as

$$\tilde{A}^{+}(0,\omega) = \sqrt{R_{HR}(\omega)}\tilde{A}^{-}(0,\omega) \tag{5.13}$$

$$\tilde{A}^{-}(L,\omega) = \sqrt{R_{OC}(\omega)}\tilde{A}^{+}(L,\omega) \tag{5.14}$$

where $R_{HR,OC}$ is the spectral profiles of the HR-FBG and the OC-FBG, respectively; $\tilde{A}^{+}$ is the forward propagation field and $\tilde{A}^{-}$ is the backward propagating field; L is the length of the fiber used in the oscillator model.

5.3.2 Parameters for simulating 25/400 μm YDF

Major parameters of the amplifier are shown in Tab.5.1. Typical values of β_2 and β_3 of modes in 25/400 μm YDFs [47, 41] are adopted. Based on the result in [47], the degenerate IM-FWM of (11,01→11,01) in 25/400 YDFs has 6 THz frequency-shift when the emission wavelength is 1080 nm. Thus, by utilizing Eqs(5.6), $\Delta\beta_1$ is calculated as 560 ps/km. Assuming that γ is proportional to $1/A_{eff,FM}$, if in 20/400 μm YDFs the FM nonlinear Kerr coefficient is typically estimated as $\gamma_{20/400} = 0.5$ W^{-1}/km [48], γ in 25/400 μm YDFs is estimated as $\gamma = 0.4$ W^{-1}/km. The normalized overlap integrals are chosen from [48, 50]. For a better demonstration of the power transition between FM and HOM, the background losses are neglected.

Table 5.1: Parameters in MM-GNLSE for amplifier simulation

Parameter	Value	Parameter	Value
λ_p	976 nm	λ_s	1080 nm
Γ_p	0.0037	τ	0.85 ms
N_0	$4 \times 10^{25}\mathrm{m}^{-3}$	L	25 m
γ	4 $\mathrm{W}^{-1}/\mathrm{km}$	$Q_{u\nu}$	0.65
$\Gamma_s^{(01)}$	0.85	$\Gamma_s^{(11)}$	1.15
$\beta_2^{(01)}$	15.6 $\mathrm{ps}^2/\mathrm{km}$	$\beta_2^{(11)}$	14 $\mathrm{ps}^2/\mathrm{km}$
$\Delta\beta_1$	560ps/km	β_3	0.04 $\mathrm{ps}^3/\mathrm{km}$

5.3.3 Simulation result

Fig.5.4 shows the spectrum of a single-mode seed laser generated from the oscillator model, whose 10 dB width is about 5 nm. Assuming there is 2% of the seed in HOM content, the power evolution of each mode and the total power along the amplifier are plotted in Fig.5.5. The multi-mode seed laser is amplified from about 980 W to 2670 W, and a 1880 W pump power is fully absorbed by a 25-meter YDF. The power of LP_{11} grows from 20 W to 72 W and LP_{01} from 960 W to 2600 W. Besides, the excitation ratio N_2/N_0 drops from 8.3% to 2.25%.

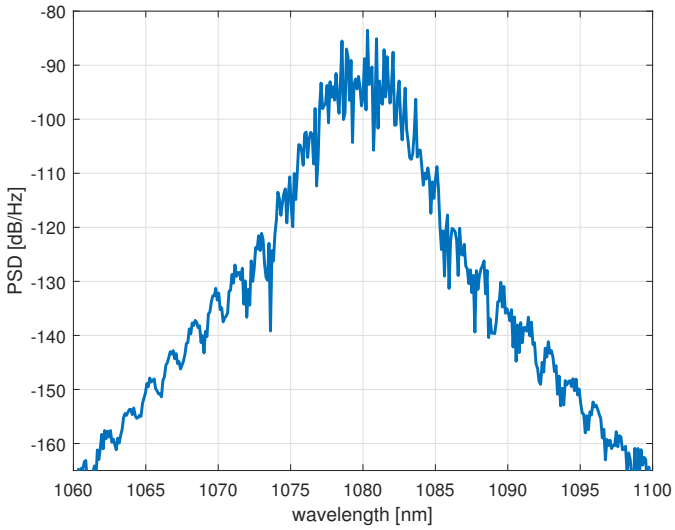

Figure 5.4: The spectrum of the FM seed laser generated from the single-mode cavity model.

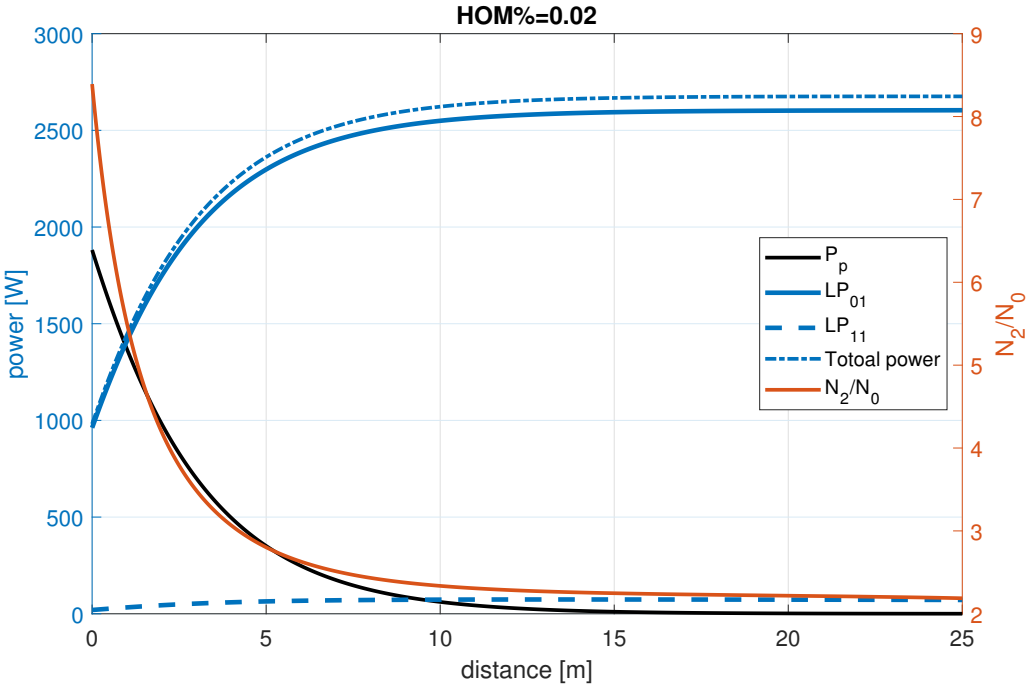

Figure 5.5: Evolution of optical powers along the fiber (left y-axis) and excitation ratio along the fiber (right y-axis). P_p is pump power; N_2/N_0 is excitation ratio along the amplifier. The HOM content in the seed laser is assumed to be 2% out of the total power of the seed laser.

The output spectra of LP_{01} and LP_{11} of the 25/400 YDF are shown in Fig.5.6. An idler at 1057 nm in FM and Stokes at 1103 nm in HOM emerge as expected. And interestingly, a second Stokes in HOM emerges at the wavelengths around 1178 nm. This second Stokes peak has about 10 THz frequency difference from the SRS Stokes at 1134 nm, which might be the degenerate IM-FWM based on the central wavelength at 1134 nm.

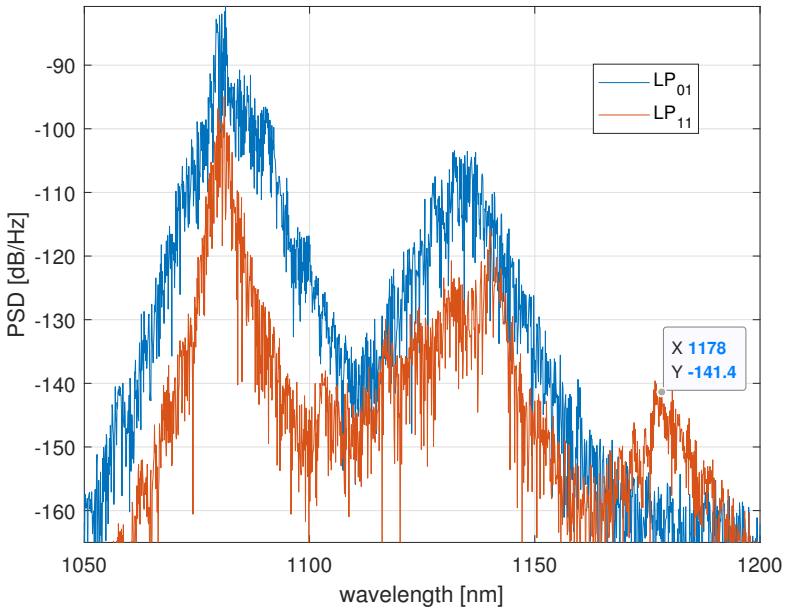

Figure 5.6: Output spectra of LP_{01} (blue) and LP_{11} (red) for the 25/400 YDF simulation. The second-order Stokes at 1178 nm is highlighted.

As proven before, the frequency shift of degenerate IM-FWM depends on Eqs(5.6), which changes along with the β_1 and β_2 of modes at different wavelength. Given the $\beta_2^{(01)}$, $\beta_2^{(11)}$ and $\Delta\beta_1$ at 1080 nm in Tab.5.1, the β_n at wavelength 1134 nm can be derived based on the below equations

$$\beta_2(\omega_0 + \Delta\omega) = \beta_3\Delta\omega + \beta_2(\omega_0) \tag{5.15}$$

$$\beta_1(\omega_0 + \Delta\omega) = \beta_3\Delta\omega^2 + \beta_2\Delta\omega + \beta_1(\omega_0) \tag{5.16}$$

The β_n values of each modes at 1134 nm are shown in Tab.5.2, and the degenerate IM-FWM frequency shift is calculated as 9.71 THz, which corresponds to the Stokes at 1177 nm and idler at 1093 nm. Therefore, the HOM second-order Stokes at 1177 nm is proven as the result from degenerate IM-FWM.

Table 5.2: Derived β_n at 1134 nm

	LP_{11}	LP_{01}
β_1 [ps/km]	-339	-1035
β_2 [ps^2/km]	10.6	12.2
$\Delta\nu$ [THz]	9.71	

5.4 Discussion

As [48] pointed out, in a two-mode high-power YDF, SRS-induced IM-WM is a dominant term in generating SRS Stokes in LP_{11} mode because it is capable of transferring power from emission wavelength of FM to the SRS Stokes of HOM. The second-order Stokes at 1177 nm in the simulation result can be regarded as the joint effect of the phenomena discussed in recent studies, which are SRS-induced IM-WM [48] and degenerate IM-FWM between LP_{01} and LP_{11} [47].

This second-order Stokes can have harmful effects on the performance of high-power fiber amplifiers. Because HOM and longer wavelengths are weakly guided in the core, the HOM second-order Stokes discussed above may suffer from high loss and thus the conversion efficiency in the amplifier is reduced. Furthermore, the beam quality is also deteriorated by the increased HOM content. Therefore, it is necessary to suppress HOM at the early stage in YDFs in order to prevent the HOM content from being accumulated at the SRS Stokes wavelength around 1134 nm, and thus generation of the HOM Stokes at 1177 nm can be avoided.

Even though the multi-mode amplifier simulation this chapter uses the same equations as [48], the HOM second-order Stokes caused by IM-FWM was not reported in [48]. This is because 20/400 μm parameters were adopted in [48], in which $\beta_2^{(01)} = 20.4\text{ps}^2/\text{km}$ and $\beta_2^{(11)} = 19.4\text{ps}^2/\text{km}$. [50] analysed the degenerate IM-FWM and analytically proved that smaller values of β_2 can lead to a larger degenerate IM-FWM efficiency in generating the corresponding Stokes and idler. Therefore, because of the adoption of larger values of β_2, the IM-FWM generation in [48] is less efficient than the result in our simulation.

To demonstrate this concept, the dispersion coefficients in previous simulations are re-

placed by $\beta_2^{(01)} = 20.4\text{ps}^2/\text{km}$ and $\beta_2^{(11)} = 19.4\text{ps}^2/\text{km}$ and $\Delta\beta_1 = 750\text{ps/km}$, where $\beta_2^{(01)}$ and $\beta_2^{(11)}$ are equal to the ones in [48] and $\Delta\beta_1$ is derived value by Eqs.(5.5). This simulation result is shown in Fig.5.7. In the output of this new simulation, even though the peak of SRS Stokes are stronger than the case in Fig.5.6, the expected HOM second-order Stokes light is much weaker than the one in Fig.5.6. Thus, the value of dispersion coefficients have an impact on the IM-FWM generation.

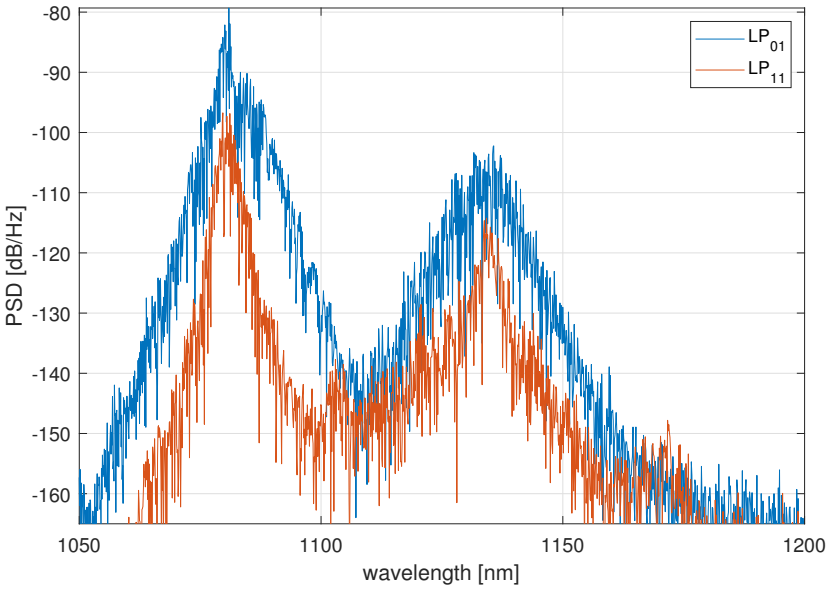

Figure 5.7: Output spectra for the YDF simulation using larger dispersion coefficients as $\beta_2^{(01)} = 20.4\text{ps}^2/\text{km}$ and $\beta_2^{(11)} = 19.4\text{ps}^2/\text{km}$.

The degenerate IM-FWM term $\partial_z A_u = A_u(z,t)|A_\nu(z,t)|^2$ is energy-conservative, which means the power from mode u can never be transferred to mode ν by this term. Thus, an adequate percentage HOM content in the seed laser (at 1080 nm in the above simulation) is needed to generate a strong IM-FWM pair at 1103 nm and 1057 nm. Therefore, in practice, by looking at the power of Stokes and idler in output spectra, the HOM content at the emission wavelength can be qualitatively estimated: the appearance of a stronger degenerate IM-FWM at 1103 nm and 1057 nm implies a higher percentage of HOM at the emission wavelength.

A variety of factors can introduced HOM content in LMA-YDFs. For instance, for an amplifier in practice, imperfect splices between combiners and the input-ends of amplifiers

can excite HOM content in seed lasers [26]. In addition, once beyond the threshold of TMI, energy can be exchanged between modes, and thus HOM at the emission wavelength can possibly increase over time. Thus, the degenerate IM-FWM can give researchers or engineers a hint to be aware of HOM content in YDFs.

5.5 Conclusion

This chapter reported intermodal couplings between LP_{01} and LP_{11} in 25/400 μm YDFs. Degenerate IM-FWM and SRS-induced IM-WM were included in this chapter. A model based on MM-GNLSE was introduced, and the principle based on phase-matching condition was given to simulate the expected IM-FWM frequency shift of the degenerate IM-FWM in 25/400 μm YDFs.

In terms of the simulation results, IM-FWM and SRS-induced IM-WM were successfully simulated. The simulation result also showed that the joint effect of IM-FWM and SRS-induced IM-WM generates a HOM second-order Stokes, which is not reported before. The harmful effects from the HOM second-order Stokes in practice were discussed. Finally, based on the simulation results, the probable experimental behaviours related to these intermodal couplings were discussed, which gave guidance to researchers and engineers when these intermodal couplings occur.

Thesis conclusion

This thesis focused on the nonlinear effects, especially SRS and IM-FWM, in CW-HPFL systems. The basic information regarding the setups and components in HPFLs were introduced in chapter 2. Models based on NLSEs were introduced in chapter 3. In chapter 4, the influence of OC-FBGs on co-pumping MOPA systems was theoretically analysed by using the models built in chapter 3. An OC-FBG with a larger BW was capable of suppressing the SRS ratio of the output laser spectrum. The underlying mechanism was that in a MOPA system, a broader OC-FBG can broaden the BW of the seed laser while only has slight impact on the power of the seed laser. Thus, because a broadened seed laser can mitigate the SRS effect in an amplifier, which had been proved experimentally and theoretically in [42], a broad OC-FBG can suppress SRS effect in a MOPA system. Furthermore, the SRS suppression by broadening the OC-FBG was found to be saturated when the broadened OC-FBG was unable to broaden the seed laser anymore. In the simulation results, the boost of backward leakage power was found to manifest the saturation of SRS suppression by broadening the OC-FBG. Based on these simulation results, this thesis proposed a suggestion that in practice, when trying to suppress SRS effect by using broadband OC-FBG, researchers or engineers should stop broadening the OC-FBG once the backward leakage power boosts.

The influence of various types of OC-FBGs on fiber oscillators were reported in chapter 4 as well. An iterative NLSE-based oscillator model was adopted for simulations. Because the iterative oscillator model's outputs, in terms of power and SRS ratio, had variation over iterations, reproducible outputs had to be achieved by averaging a number of iterations. In comparison with a broadband OC-FBG, a fiber oscillator with a narrowband OC-FBG had a lower backward propagation power, a better conversion efficiency and a larger SRS ratio. Furthermore, CM-FBGs, which were represented by multi-peak spectral profiles, were

simulated by using the NLSE-based oscillator model for the first time. The simulation results agreed with the experimental results in [39]. For a CM-FBG with the same spectral envelope of a broad OC-FBG, the CM-FBG had the same SRS suppression capacity as the broad one, whereas the backward leakage power for the CM-FBG is mitigated. In the simulation results, the interval between peaks in the multi-peak spectral profile of a CM-FBG played an important role in the performance of the CM-FBG. The capacity of suppressing SRS gradually vanished when the distribution of the peaks for a CM-FBG became sparser. At the same time, the sparse-distributed CM-FBG's performance approached to a narrow OC-FBG.

In chapter 5, intermodal impairments between LP_{01} and LP_{11} in 25/400 μm YDFs were reported. A model based on MM-GNLSE was introduced to simulated the coupling between modes. Furthermore, based on the theory of intermodal parametric process for IM-FWM, the principle to model the expected IM-FWM Stokes and idler was introduced. Using this model, the recently discussed intermodal impairments, including SRS-induced IM-WM [48] and IM-FWM[47], were successfully simulated. Besides, a HOM second-order Stokes emerges in the simulation, which was proven to be the joint effect of SRS-induced IM-WM and IM-FWM. To the best of our knowledge, this was the first work simulating the IM-FWM phenomenon in LMA-YDFs, and the HOM second-order Stokes is also a novel intermodal impairment in high-power fiber amplifiers.

Regarding the future works, the models in the thesis can be used to simulate and optimize novel experiments. For instance, SRS suppression effect of chirped-tilted FBGs reported in [52, 53, 34] can be simulated by using NLSE-based models, so that an optimal design of chirped-tilted FBGs can be possibly obtained in order to improve the performance of HPFLs. In addition, OC-FBGs' spectral profiles are assumed to be in regular shapes in the simulations in this thesis, but the reflectivity profiles of FBGs are measured to be irregular and slightly rippling [27]. Thus, the measured spectral profiles of FBGs can be adopted in simulations in order to obtain simulation results closer to experiments. For the part of intermodal couplings, the work in chapter 5 can be improved by considering more modes or different kind of parametric processes in the model.

Bibliography

[1] D. Richardson, J. Nilsson, and W. Clarkson, "High power fiber lasers: current status and future perspectives," *JOSA B*, vol. 27, no. 11, pp. B63–B92, 2010.

[2] J. Nilsson and D. N. Payne, "High-power fiber lasers," *Science*, vol. 332, no. 6032, pp. 921–922, 2011.

[3] M. Bass, *Laser materials processing*, vol. 3. Elsevier, 2012.

[4] M. N. Zervas and C. A. Codemard, "High power fiber lasers: a review," *IEEE Journal of selected topics in Quantum Electronics*, vol. 20, no. 5, pp. 219–241, 2014.

[5] G. P. Agrawal, "Nonlinear fiber optics," Elsevier, 2013.

[6] C. Stihler, C. Jauregui, A. Tünnermann, and J. Limpert, "Modal energy transfer by thermally induced refractive index gratings in yb-doped fibers," *Light: Science & Applications*, vol. 7, no. 1, p. 59, 2018.

[7] C. Stihler, C. Jauregui, A. Tünnermann, and J. Limpert, "Phase-shift evolution of the thermally-induced refractive index grating in high-power fiber laser systems induced by pump-power variations," *Optics express*, vol. 26, no. 15, pp. 19489–19497, 2018.

[8] C. Stihler, C. Jauregui, A. Tünnermann, and J. Limpert, "Towards the control of the modal energy transfer in transverse mode instabilities," in *Proc. of SPIE Vol*, vol. 10512, pp. 1051204–1, 2018.

[9] R. Tao, X. Wang, and P. Zhou, "Comprehensive theoretical study of mode instability in high-power fiber lasers by employing a universal model and its implications," *IEEE Journal of Selected Topics in Quantum Electronics*, vol. 24, no. 3, pp. 1–19, 2018.

[10] C. Jauregui, C. Stihler, A. Tünnermann, and J. Limpert, "Pump-modulation-induced beam stabilization in high-power fiber laser systems above the mode instability threshold," *Optics express*, vol. 26, no. 8, pp. 10691–10704, 2018.

[11] P. Yan, X. Wang, D. Li, Y. Huang, J. Sun, Q. Xiao, and M. Gong, "High-power 1018 nm ytterbium-doped fiber laser with output of 805 w," *Optics letters*, vol. 42, no. 7, pp. 1193–1196, 2017.

[12] P. Yan, X. Wang, Z. Wang, Y. Huang, D. Li, Q. Xiao, and M. Gong, "A 1150-w 1018-nm fiber laser bidirectional pumped by wavelength-stabilized laser diodes," *IEEE Journal of Selected Topics in Quantum Electronics*, vol. 24, no. 3, pp. 1–6, 2018.

[13] Y. Wang and H. Po, "Dynamic characteristics of double-clad fiber amplifiers for high-power pulse amplification," *Journal of lightwave technology*, vol. 21, no. 10, pp. 2262–2270, 2003.

[14] W. Tian, Z. Wang, L. Wei, Y. Peng, J. Zhang, Z. Zhu, J. Zhu, H. Han, Y. Jia, L. Zheng, *et al.*, "Diode-pumped kerr-lens mode-locked yb: Lyso laser with 61fs pulse duration," *Optics express*, vol. 22, no. 16, pp. 19040–19046, 2014.

[15] T. Schreiber, A. Liem, E. Freier, C. Matzdorf, R. Eberhardt, C. Jauregui, J. Limpert, and A. Tünnermann, "Analysis of stimulated raman scattering in cw kw fiber oscillators," in *Fiber Lasers XI: Technology, Systems, and Applications*, vol. 8961, p. 89611T, International Society for Optics and Photonics, 2014.

[16] B. Yang, H. Zhang, C. Shi, R. Tao, R. Su, P. Ma, X. Wang, P. Zhou, X. Xu, and Q. Lu, "3.05 kw monolithic fiber laser oscillator with simultaneous optimizations of stimulated raman scattering and transverse mode instability," *Journal of Optics*, vol. 20, no. 2, p. 025802, 2018.

[17] Y. Wang, C.-Q. Xu, and H. Po, "Analysis of raman and thermal effects in kilowatt fiber lasers," *Optics communications*, vol. 242, no. 4-6, pp. 487–502, 2004.

[18] Y. Mashiko, H. Nguyen, M. Kashiwagi, T. Kitabayashi, K. Shima, and D. Tanaka, "2 kw single-mode fiber laser with 20-m long delivery fiber and high srs suppression," in *Fiber*

Lasers XIII: Technology, Systems, and Applications, vol. 9728, p. 972805, International Society for Optics and Photonics, 2016.

[19] P. Leproux, S. Février, V. Doya, P. Roy, and D. Pagnoux, "Modeling and optimization of double-clad fiber amplifiers using chaotic propagation of the pump," *Optical Fiber Technology*, vol. 7, no. 4, pp. 324–339, 2001.

[20] G. Brochu, A. Villeneuve, M. Faucher, M. Morin, F. Trépanier, and R. Dionne, "Srs modeling in high power cw fiber lasers for component optimization," in *Components and Packaging for Laser Systems III*, vol. 10085, p. 100850N, International Society for Optics and Photonics, 2017.

[21] Q. Fang, J. Li, W. Shi, Y. Qin, Y. Xu, X. Meng, R. A. Norwood, and N. Peyghambarian, "5 kw near-diffraction-limited and 8 kw high-brightness monolithic continuous wave fiber lasers directly pumped by laser diodes," *IEEE Photonics Journal*, vol. 9, no. 5, pp. 1–7, 2017.

[22] C. Shi, R. T. Su, H. W. Zhang, B. L. Yang, X. L. Wang, P. Zhou, X. J. Xu, and Q. S. Lu, "Experimental study of output characteristics of bi-directional pumping high power fiber amplifier in different pumping schemes," *IEEE Photonics Journal*, vol. 9, no. 3, pp. 1–10, 2017.

[23] L. Yin, M. Yan, Z. Han, H. Wang, H. Shen, and R. Zhu, "High power cladding light stripper using segmented corrosion method: theoretical and experimental studies," *Optics express*, vol. 25, no. 8, pp. 8760–8776, 2017.

[24] A. Wetter, M. Faucher, and B. Sévigny, "High power cladding light strippers," in *Fiber Lasers V: Technology, Systems, and Applications*, vol. 6873, p. 687327, International Society for Optics and Photonics, 2008.

[25] K. Hejaz, M. Shayganmanesh, A. Roohforouz, R. Rezaei-Nasirabad, A. Abedinajafi, S. Azizi, and V. Vatani, "Transverse mode instability threshold enhancement in yb-doped fiber lasers by cavity modification," *Applied optics*, vol. 57, no. 21, pp. 5992–5997, 2018.

[26] S. Moon, D.-Y. Kim, and T.-J. Ahn, "Spliced-fiber mode filter for 1060-nm single-mode transmission," *Optics Communications*, vol. 283, no. 20, pp. 3957–3961, 2010.

[27] W. Mohammed and X. Gu, "Fiber bragg grating in large-mode-area fiber for high power fiber laser applications," *Applied optics*, vol. 49, no. 28, pp. 5297–5301, 2010.

[28] E. L. M. R. S. U. J. K. K. S. H. B. Martin Becker, Sven Brückner, "Fiber bragg grating inscription with uv femtosecond exposure and two beam interference for fiber laser applications," 2010.

[29] J. Aubrecht, A. Theodosiou, P. Peterka, I. Kašík, F. Todorov, O. Moravec, P. Honzátko, and K. Kalli, "Monolithic er/yb double-clad fibre laser with fbg inscribed using the direct-write plane-by-plane fs-laser inscription method (conference presentation)," in *Fiber Lasers and Glass Photonics: Materials through Applications*, vol. 10683, p. 1068304, International Society for Optics and Photonics, 2018.

[30] J. Fiebrandt, E. Lindner, S. Brückner, M. Becker, A. Schwuchow, M. Rothhardt, and H. Bartelt, "Growth characterization of fiber bragg gratings inscribed in different rare-earth-doped fibers by uv and vis femtosecond laser pulses," *Optics Communications*, vol. 285, no. 24, pp. 5157–5162, 2012.

[31] A. Fuerbach, G. Bharathan, S. Antipov, M. Ams, R. Williams, D. Hudson, R. Woodward, and S. Jackson, "Line-by-line femtosecond fbg inscription for innovative fiber lasers," in *Bragg Gratings, Photosensitivity and Poling in Glass Waveguides and Materials*, pp. BW3A–6, Optical Society of America, 2018.

[32] F. Becker, B. Neumann, L. Winkelmann, S. Belke, S. Ruppik, U. Hefter, B. Köhler, P. Wolf, and J. Biesenbach, "Multi-kw cw fiber oscillator pumped by wavelength stabilized fiber coupled diode lasers," in *Fiber Lasers X: Technology, Systems, and Applications*, vol. 8601, p. 860131, International Society for Optics and Photonics, 2013.

[33] A. Salokatve, "Means of coupling light into optical fibers and methods of manufacturing a coupler," Aug. 2 2011. US Patent 7,991,255.

[34] M. Wang, Q. Hu, L. Liu, Z. Wang, and X. Xu, "Suppression of stimulated raman scattering in a monolithic fiber laser oscillator using chirped and tilted fiber bragg gratings," in *High-Power Lasers and Applications IX*, vol. 10811, p. 108110V, International Society for Optics and Photonics, 2018.

[35] Q. Xiao, P. Yan, H. Ren, X. Chen, and M. Gong, "A side-pump coupler with refractive index valley configuration for fiber lasers and amplifiers," *Journal of Lightwave Technology*, vol. 31, no. 16, pp. 3015–3022, 2013.

[36] Z. Li, Z. Huang, X. Xiang, X. Liang, H. Lin, S. Xu, Z. Yang, J. Wang, and F. Jing, "Experimental demonstration of transverse mode instability enhancement by a counter-pumped scheme in a 2 kw all-fiberized laser," *Photonics Research*, vol. 5, no. 2, pp. 77–81, 2017.

[37] B. Yang, H. Zhang, C. Shi, X. Wang, P. Zhou, X. Xu, J. Chen, Z. Liu, and Q. Lu, "Mitigating transverse mode instability in all-fiber laser oscillator and scaling power up to 2.5 kw employing bidirectional-pump scheme," *Optics Express*, vol. 24, no. 24, pp. 27828–27835, 2016.

[38] Z. S. Eznaveh, G. Lopez-Galmiche, E. Antonio-Lopez, and R. A. Correa, "Bi-directional pump configuration for increasing thermal modal instabilities threshold in high power fiber amplifiers," in *Fiber Lasers XII: Technology, Systems, and Applications*, vol. 9344, p. 93442G, International Society for Optics and Photonics, 2015.

[39] H. Xu, M. Jiang, C. Shi, P. Zhou, G. Zhao, and X. Gu, "Spectral shaping for suppressing stimulated-raman-scattering in a fiber laser," *Applied optics*, vol. 56, no. 12, pp. 3538–3542, 2017.

[40] W. Liu, W. Kuang, L. Huang, and P. Zhou, "Modeling of the spectral properties of cw yb-doped fiber amplifier and experimental validation," *Laser Physics Letters*, vol. 12, no. 4, p. 045104, 2015.

[41] W. Liu, P. Ma, H. Lv, J. Xu, P. Zhou, and Z. Jiang, "General analysis of srs-limited

high-power fiber lasers and design strategy," *Optics express*, vol. 24, no. 23, pp. 26715–26721, 2016.

[42] W. Liu, P. Ma, H. Lv, J. Xu, P. Zhou, and Z. Jiang, "Investigation of stimulated raman scattering effect in high-power fiber amplifiers seeded by narrow-band filtered superfluorescent source," *Optics express*, vol. 24, no. 8, pp. 8708–8717, 2016.

[43] S. Turitsyn, A. Bednyakova, M. Fedoruk, A. Latkin, A. Fotiadi, A. Kurkov, and E. Sholokhov, "Modeling of cw yb-doped fiber lasers with highly nonlinear cavity dynamics," *Optics Express*, vol. 19, no. 9, pp. 8394–8405, 2011.

[44] V. Bock, A. Liem, T. Schreiber, R. Eberhardt, and A. Tünnermann, "Explanation of stimulated raman scattering in high power fiber systems," in *Fiber Lasers XV: Technology and Systems*, vol. 10512, p. 105121F, International Society for Optics and Photonics, 2018.

[45] A. Bednyakova, O. Gorbunov, M. Politko, S. Kablukov, S. Smirnov, D. Churkin, M. Fedoruk, and S. Babin, "Generation dynamics of the narrowband yb-doped fiber laser," *Optics express*, vol. 21, no. 7, pp. 8177–8182, 2013.

[46] J. Wang, D. Yan, S. Xiong, B. Huang, and C. Li, "High power all-fiber amplifier with different seed power injection," *Optics Express*, vol. 24, no. 13, pp. 14463–14469, 2016.

[47] L. Yin, Z. Han, H. Shen, and R. Zhu, "Suppression of inter-modal four-wave mixing in high-power fiber lasers," *Optics Express*, vol. 26, no. 12, pp. 15804–15818, 2018.

[48] W. Liu, P. Ma, C. Shi, P. Zhou, and Z. Jiang, "Theoretical analysis of the srs-induced mode distortion in large-mode area fiber amplifiers," *Optics Express*, vol. 26, no. 12, pp. 15793–15803, 2018.

[49] F. Poletti and P. Horak, "Description of ultrashort pulse propagation in multimode optical fibers," *JOSA B*, vol. 25, no. 10, pp. 1645–1654, 2008.

[50] Y. Xiao, R.-J. Essiambre, M. Desgroseilliers, A. M. Tulino, R. Ryf, S. Mumtaz, and G. P. Agrawal, "Theory of intermodal four-wave mixing with random linear mode coupling in few-mode fibers," *Optics express*, vol. 22, no. 26, pp. 32039–32059, 2014.

[51] R.-J. Essiambre, M. A. Mestre, R. Ryf, A. H. Gnauck, R. W. Tkach, A. R. Chraplyvy, Y. Sun, X. Jiang, and R. Lingle, "Experimental investigation of inter-modal four-wave mixing in few-mode fibers," *IEEE Photonics Technology Letters*, vol. 25, no. 6, pp. 539–542, 2013.

[52] M. Wang, Y. Zhang, Z. Wang, J. Sun, J. Cao, J. Leng, X. Gu, and X. Xu, "Fabrication of chirped and tilted fiber bragg gratings and suppression of stimulated raman scattering in fiber amplifiers," *Optics express*, vol. 25, no. 2, pp. 1529–1534, 2017.

[53] M. Wang, Z. Li, L. Liu, Z. Wang, X. Gu, and X. Xu, "Fabrication of chirped and tilted fiber bragg gratings on large-mode-area doubled-cladding fibers by phase-mask technique," *Applied optics*, vol. 57, no. 16, pp. 4376–4380, 2018.